

# *International Review of Civil Engineering (IRECE)*

## **Contents**

<b>Effect of Variation in Temperature on Thermal Conductivity of Compressed Earth Block (CEBs) in Dry and Ambient States</b>	87
<i>by N. Zakhm, K. Gueraoui, H. Bouabid, M. Cherraj, M. Belcadi</i>	
<b>Effect of Soil Drainage on California Bearing Ratio of Soaked Clay</b>	92
<i>by Robert G. Nini, Michel Y. Chalhoub</i>	
<b>Relationship between Bituminous Mastic and Mix Asphalt Properties</b>	96
<i>by Wahib Youssef, Abidi My Larbi</i>	
<b>A Nonlinear Control Method for Autonomous Navigation Guidance</b>	102
<i>by G. Carloni, K. Bousson</i>	
<b>A Dynamic Finite Element for Coupled Extensional-Torsional Vibration of Uniform Composite Thin-Walled Beams</b>	114
<i>by S. M. Hashemi, A. Roach</i>	



# Effect of Variation in Temperature on Thermal Conductivity of Compressed Earth Block (CEBs) in Dry and Ambient States

N. Zakham<sup>1,2</sup>, K. Gueraoui<sup>1,3</sup>, H. Bouabid<sup>2</sup>, M. Cherraj<sup>1</sup>, M. Belcadi<sup>1</sup>

**Abstract** – In our days, the hydrothermal behavior of building materials raises a deep interest. The search for energy savings, by using techniques of optimization of thermo-physiques characteristics of materials of the building walls, is grown. It is important to measure the local thermal conductivity in such materials when they are facing changes in temperature gradients and humidity. Our primary objective is to determine thermal conductivity ( $\lambda$ ) of ambient and dry material of compressed earth blocks stabilized by cement (CEBs). Usually this characteristic is measured experimentally and numerically by using the transfer heat into compressed earth block (CEBs). The numerical model used to solve the 2-D is based on the finite volume method. The obtained algebraic systems are solved by the double scanning mesh method. The measurement technique used to determine the thermal conductivity is called 'hot rings method'. **Copyright © 2016 Praise Worthy Prize S.r.l. - All rights reserved.**

**Keywords:** Compressed Earth Blocks, Thermal Conductivity, Cement, Temperature, Hot Rings Method

## Nomenclature

$C_p$	Specific heat [J /kg K]
$K$	Thermal conductivity [W/m K]
$\dot{q}$	Heat flux [W m <sup>2</sup> ]
$r$	Radial coordinate
$T$	Temperature [°C]
$t$	Heating time [S]
$z$	Axial coordinate
$\rho$	Bulk mass [kg/m <sup>3</sup> ]

## I. Introduction

The main objective of many studies made in several countries was to manufacture the building at low costs.

The stabilization of compressed earth blocks (CEBs) allows to improve the physical properties of the block and to increase its hardness without energetic costs.

The stabilizer can be the cement, lime, sawdust, gypsum and fiber etc. The introduction of this stabilizer in earth block has a strong influence on the thermal property of the materials according to the percentage of the stabilizer and the water.

Azakine Sindanne and al [1] studied experimentally the thermal conductivity of earth block stabilized by various stabilizer (cement, lime and sawdust), by hot wire method. The incorporation of stabilizers was conducted in CEBs for different percentages: 4%, 8% and 12% for each type of stabilizer.

Thermal conductivities of CEBs increased with the increase of the percentages of cement and lime and decreased with the increasing of sawdust percentage.

Meukam and al [2] carried out an experimental study on the thermal properties of bricks made by lateritic soil.

In order to limit the water absorption and to increase the durability, cement has been added to the earth blocks.

The experiment showed that cement content up to 10% is enough to limit the water absorption. The effect of the addition of natural pozzolan or sawdust is the decrease of their thermal conductivity. It has been shown that water content is the major variable affecting the thermo-physical properties of the tested samples.

The coefficients of thermal conductivity and thermal diffusivity were strongly influenced by the material's water content.

Coquard and al [3] studied the numerical model developed to solve the 2-D heat transfer around the ring taking into account the conduction–radiation and the inertia of the element.

Some numerical and experimental results showed that the classical hot-ring apparatus are poorly adapted to the measurements on low-density insulators owing to the thermal inertia of the elements. However, they developed a modified identification procedure eliminating the influence of the inertia of the apparatus on the measured thermal conductivity.

The objective of this work is to study experimentally and numerically the transfer of heat by the hot-ring method using two different states of the samples of compressed earth block stabilized by cement: dry state and ambient state.

The samples have cylindrical forms. The temperature field is calculated numerically using the finite volume method, implicit in time in r-direction and explicit in z-direction using FORTRAN program.

## II. Studied Materials

The materials used for the three types of compressed earth block are: soil, cement and aggregates (different granular mixtures) which have the following characteristics (Tables I, II).

TABLE I  
THE GRANULAR FRACTION OF EARTH FEZ

Granular fraction (%)				
gravels	large sand	Thin sand	Silt	Clay
28	30	22	12	8

TABLE II  
FORMULATION OF THE SAMPLES STUDIED

The samples	Cement content (%)	Height(m)	Bulk density $\rho(\text{kg/m}^3)$	Compacting pressure (MPa)
Sample 1	4	0,125	1815,28	2
Sample 2	7	0,123	1747,71	2
Sample 3	4	0,123	1860,99	2



Fig. 1. The samples into the oven

These three samples have been studied in cylindrical forms; each sample is divided in two. Samples 1 and 2 are in dry state while sample 3 is in ambient state.

## III. Data and Method

In order to identify experimentally the sources of heat, heat flux or thermo-physical parameters, the techniques of the hot ring method require the measurement of the temperature in non permanent regime and in specific points on the surface of samples. The most commonly used techniques are the thermocouple.

This heat flux is dissipated in the material and arrives within a certain time in the center of the ring. The principle of the shock sensor is to produce locally a very low heat on the material (few degrees above the ambient temperature) and to measure the elevation of the temperature over time (for several minutes) [4].



Fig. 2. The kapton slab of the hot-ring apparatus



Fig. 3. The kapton slab of the hot-ring apparatus in the middle the sample

## IV. Numerical Method

The Transfer of energy in the material, in two dimensional cylindrical coordinates, is governed by the following heat equation [5]-[7]:

$$\rho C_p \frac{\partial T}{\partial t} = k \frac{1}{r} \left( \frac{\partial}{\partial r} \left( r \frac{\partial T}{\partial r} \right) \right) + \frac{\partial^2 T}{\partial z^2} + \dot{q} \quad (1)$$

The Initial conditions are:

$$t \leq 0 \quad T(r, z, t) = T_\infty \quad \forall r \text{ and } \forall z$$

with the following boundary conditions:

$$r = 0, \quad \forall z \quad \frac{\partial T}{\partial r} = 0$$

$$z = -\frac{H}{2} \text{ and } z = +\frac{H}{2}, \quad T = T_\infty$$

$$\forall z \text{ and } r = R, \quad T = T_\infty$$

Recently, numerous methods have been developed to solve the irradiative transfer equation (RTE) in multidimensional cylindrical configurations. For our case, we opted for a finite volumes method [8], [25].

The heat equation (Eq. (1)) can be expressed in the following form:

$$\begin{aligned} \rho C_p (T_p - T_p^o) r_p \Delta r \Delta z = & \\ k \left\{ \left[ r \frac{\partial T}{\partial r} \right]_e - \left[ r \frac{\partial T}{\partial r} \right]_o \right\} \Delta z \Delta t + & \quad (2) \\ + k \left\{ \left[ \frac{\partial T}{\partial z} \right]_n - \left[ \frac{\partial T}{\partial z} \right]_s \right\} r_p \Delta r \Delta t + \dot{q} r_p \Delta r \Delta z \Delta t & \end{aligned}$$

$$\begin{aligned} \rho C_p (T_p - T_p^o) r_p \Delta r \Delta z = & \\ \left\{ \frac{(r_E + r_p)(T_E - T_p)}{2 \Delta r} - \frac{(r_p + r_o)(T_p - T_o)}{2 \Delta r} \right\} \Delta z \Delta t + & \quad (3) \\ + k \left\{ \left[ \frac{(T_N - T_p)}{\Delta z} \right]_n - \left[ \frac{(T_p - T_S)}{\Delta z} \right]_s \right\} r_p \Delta r \Delta t + & \\ + \dot{q} r_p \Delta r \Delta z \Delta t & \end{aligned}$$

$$\begin{aligned} T_p \left( \rho C_p r_p \Delta r \Delta z + \frac{k}{2 \Delta r} \Delta z \Delta t (r_E + 2r_p + r_o) + \right. & \\ \left. + \frac{2k}{\Delta z} \Delta r \Delta t r_p \right) = & \\ T_E \left( k \frac{(r_E + r_p)}{2 \Delta r} \Delta z \Delta t \right) + T_o \left( k \frac{(r_p + r_o)}{2 \Delta r} \Delta z \Delta t \right) + & \quad (4) \\ + T_N \left( \frac{k}{\Delta z} \Delta r \Delta t r_p \right) + T_S \left( \frac{k}{\Delta z} \Delta r \Delta t r_p \right) + \dot{q} r_p \Delta r \Delta z \Delta t & \end{aligned}$$

The final algebraic equation is given by the following expression:

$$a_p T_p = a_E T_E + a_o T_o + a_N T_N + a_S T_S + b_o \quad (5)$$

with:

$$\begin{aligned} a_E &= \frac{k}{2 \Delta r} \Delta z \Delta t (r_E + r_p) \\ a_o &= \frac{k}{2 \Delta r} \Delta z \Delta t (r_p + r_o), \quad a_N = \frac{k}{\Delta z} \Delta r \Delta t r_p \\ a_N &= \frac{k}{\Delta z} \Delta r \Delta t r_p, \quad a_S = \frac{k}{\Delta z} \Delta r \Delta t r_p \\ a_p &= a_p^o + a_E + a_o + a_N + a_S, \quad a_p^o = \rho C_p r_p \Delta r \Delta z \end{aligned}$$

$$\begin{aligned} b_o &= a_p^o T_p^o + \dot{q} r_p \Delta r \Delta z \Delta t \\ \rho C_p (T_p - T_p^o) r_p \Delta r \Delta z &= k \left\{ \frac{(r_E + r_p)(r_E - r_p)}{2 \Delta r} + \right. \\ & \left. - \frac{(r_p + r_o)(r_p - r_o)}{2 \Delta r} \right\} \Delta z \Delta t + \\ + k \left\{ \left[ \frac{T_N - T_p}{\partial z} \right]_n - \left[ \frac{T_p - T_S}{\partial z} \right]_s \right\} r_p \Delta r \Delta t + \dot{q} r_p \Delta r \Delta z \Delta t & \end{aligned}$$

This system of algebraic equations is applied only to areas not influenced by the boundary conditions.

## V. Results and Discussions

We have used the hot-ring apparatus previously and measured the temperature rise at the center of the ring for each of the CEBs samples presented. We measured the temperature profile for different time with different heating time and different power. The thermal diffusivity was determined using the following relationship:

$$\alpha = \frac{K}{\rho C_p} \quad (6)$$

The Table III shows the variation of the thermal conductivity of the three tested materials with cement dosage. The thermal conductivity increases with the cement dosage. A moist material therefore conducts less heat than the dry material. This phenomenon is due to the fact that the soil is a porous medium [26]-[31].

TABLE III  
THE RESULTS OF THERMAL CONDUCTIVITY (K), SPECIFIC HEAT ( $C_p$ ) AND THERMAL DIFFUSIVITY FOR CEBs SAMPLES

The samples	Sample 1	Sample 2	Sample 3
Cement content (%)	4	7	4
Power (W)	2	2	2
Heating time(s)	400	400	400
Mesure Time(s)	500	500	500
Specific heat(J/kg, K)	968,557	1090,623	941,783
Thermal conductivity (W/mK)	0,733	0,813	0,739
Thermal diffusivity(m <sup>2</sup> /s)	4,17 E-07	4,26E-07	4,22E-07

It can be noted in Fig. 4 that the temperature during the test increased slowly until its maximum reached at 450 s. After 450 s, the hot-ring apparatus was turned off to induce the temperature decreasing the phase of a sample of CEBs. The numerical and experimental results were in good agreement. In this case the ambient temperature was 21 °C.

In Fig. 5 it can be seen that the temperature during the test increased slowly until its maximum reached at 480 s.

After 480 s, the hot-ring apparatus was turned off to induce the temperature decreasing the phase of a sample of CEBs. The numerical and experimental results were in good agreement. In this case the ambient temperature was 22 °C.

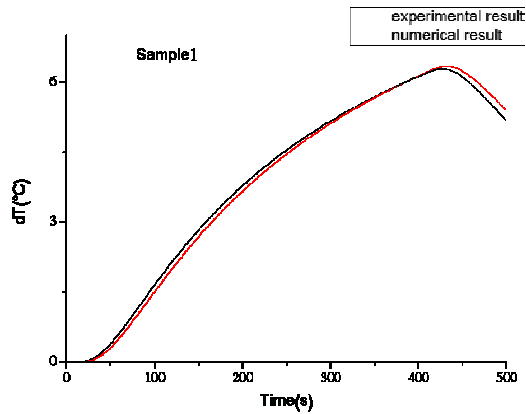


Fig. 4. Comparison between experimental and numerical evolution of the temperature for the sample 1 of the hot-ring apparatus

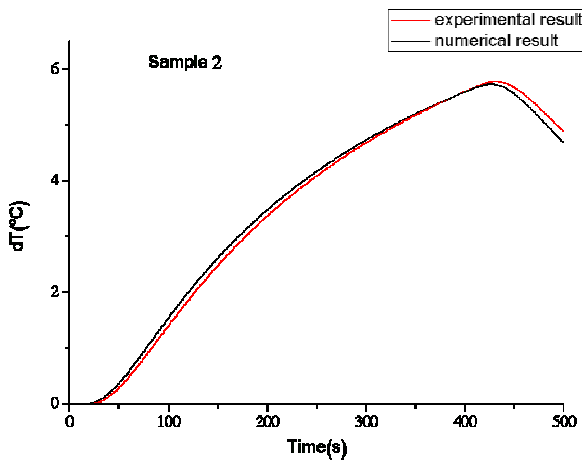


Fig. 5. Comparison between experimental and numerical evolution of the temperature for the sample 2 of the hot-ring apparatus

It can be noted in Fig. 6 that the temperature during the test increased slowly until its maximum reached at 450 s. After 450 s, the hot-ring apparatus was turned off to induce the temperature decreasing the phase of a sample of CEBs. The numerical and experimental results were in good agreement. In this case the ambient temperature was 22 °C.

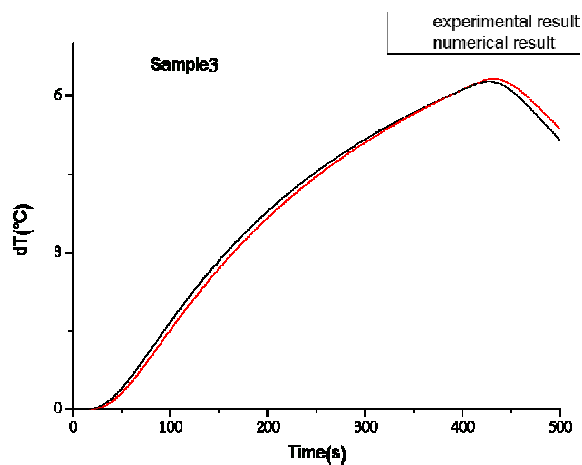


Fig. 6. Comparison between experimental and numerical evolution of the temperature for the sample 3 of the hot-ring apparatus

## VI. Conclusion

The comfort of the building and the quality of indoor air are becoming important parameters in the selection of building materials use for the buildings. The work aimed to determine the thermo-physical properties of compressed earth bloc with respect cement stabilization.

The hot-ring method is a transient technique for measuring the thermal conductivity of materials whose principle fits the geometrical dimensions of the sample.

The experimental results fit the numerical results.

The variation of temperature has affected the cement dosage of the dry and ambient states of CEBs.

## References

- [1] Azakine Sindanne S, Ntamack GE , Lemanle Sanga RP , Moubeke CA , Kelmamo Sallaboui ES , Bouabid H , Mansouri K, D'Ouazzane SC Thermophysical characterization of earth blocks stabilized by cement, sawdust and lime; *J. Build. Mater. Struct.* (2014) 1: 58-64.
- [2] P. Meukam., Y. Jannot, A. Noumowe, T.C. Kofane, Thermo physical characteristics of economical building materials, *Construction and Building Materials* 18 (2004) 437–443.
- [3] R. Coquard, D. Baillis, D. Quenard , Experimental and theoretical study of the hot-ring method applied to low-density thermal insulators; *International Journal of Thermal Sciences* 47 (2008) 324–338.
- [4] Márcio Buson, Nuno Lopes, Humberto Varum, Rosa Maria Sposto and Paulo Vila Real, *Fire resistance of walls made of soil-cement and Kraftterra compressed earth blocks*, FIRE AND MATERIALS .Fire Mater. (2012).Published online in Wiley Online Library (wileyonlinelibrary.com). DOI: 10.1002/fam.2148.
- [5] Belcadi M., El Rhaleb H., Gueraoui K., Driouich M., Hybridization microwave and laser for melting of ceramic surface, *Adv. Studies Theo. Phys.*, 8 (2014).
- [6] Gueraoui K., Hammoumi A., Zeggwagh, G.(1996), Ecoulements pulsés de fluides inélastiques en conduites déformables poreuses et anisotropes, *C.R. Acad. Sci.*, Paris, 323, série B, pp. 825-832.
- [7] Abdelhak Ghoul, Kamal Gueraoui, Myrieme Walid, Ilham Aberdane, Abdellah El Hammoumi, Mohammed Kerroum, Gamal Zeggwagh, Yehia Mohammed Haddad, Numerical Study of Pollutant Propagation Process in Homogeneous Porous Unsaturated Media, (2009) *International Review of Mechanical Engineering (IREME)*, 3 (3), pp. 358-362.
- [8] M. Driouich, K. Gueraoui, Y. M. Haddad, A. El Hammoumi, M. Kerroum, O. Fassi Fehri, Mathematical modeling of non permanent flows of molten polymers, (2010) *International Review of Mechanical Engineering (IREME)*, 4 (6), pp. 689-694.
- [9] Men-la-yakhaf, S. , Gueraoui, K., Driouich, M.,(2014), Numerical and Mathematical Modeling of Reactive Mass Transfer and Heat Storage Installations of Argan Waste, *Advanced Studies in Theoretical Physics*, Vol. 8, no. 10, 485-498.
- [10] Belcadi, M., El Rhaleb, H., Gueraoui, K., Driouich, M., Combined Processes: Laser Assisted Microwave Sintering of Alumina, (2013) *International Review of Mechanical Engineering (IREME)*, 7 (7), pp. 1451-1458.
- [11] Men-la-yakhaf, S., Gueraoui, K., Maaouni, A., Driouich, M., Numerical and Mathematical Modeling of Reactive Mass Transfer and Heat Storage Installations of Argan Waste, (2014) *International Review of Mechanical Engineering (IREME)*, 8 (1), pp. 236-240.
- [12] A. Saad, A. Echchelh, F. Lahlou, K. Gueraoui, P.Cardot, The Kinematic Elution of 99mTc Radio Labelled Red Blood Cells in a Channel of Gravitational Field Flow Fractionation (GrFFF), (2008) *International Review of Mechanical Engineering (IREME)*, 2 (2), pp. 233-240.
- [13] Belcadi M., El Rhaleb H., Gueraoui K., Driouich M., Dhiri A, *Numerical Simulation of Microwaves Assisted Laser Melting*

- Alumina*, vol. 9, N. 5 September 2015, pp. 429-437.
- [14] Chammami R., Taibi M., Hami M., Gueraoui K., Zeggwagh G., Influence of the kind of duct on two-fluid pulsatile flows model. Application to the microcirculation, *Houille Blanche* (2001).
- [15] Taibi M., Chammami R., Kerroum M., Gueraoui K., El Hammoumi A., Zeggwagh G., *Pulsating flow of two phases in deformable or rigid tubes*, ITBM-RBM (2002).
- [16] EL-Touroug, H., Gueraoui, K., Hassanain, N., Driouich, M., Men-La-Yakhaf, S., Numerical Modeling of the Phenomenon of Crystallization of Incompressible Fluid Flows into Rigid Pipes. Application to Polymer Melts, (2015) *International Review on Modelling and Simulations (IREMOS)*, 8 (1), pp. 99-103.
- [17] Ilham Aberdane, Kamal Gueraoui, Mohammed Taibi, Abdelhak Ghouli, Abdellah El Hammoumi, Mohammed Cherraj, Mohammed Kerroum, Myrieme Walid, Omar Fassi Fihri, Yehia Mohammed Haddad, Two-Dimensional Theoretical and Numerical Approach of Pollutant Transport in the Lowest Layers of the Atmosphere, (2009) *International Review of Mechanical Engineering (IREME)*, 3 (4), pp. 494-502.
- [18] M. Sammouda, K. Gueraoui, M. Driouich, A. El Hammoumi, A. Iben Brahim, The Variable Porosity Effect on the Natural Convection in a non-Darcy Porous Media, (2011) *International Review on Modelling and Simulations (IREMOS)*, 4 (5), pp. 2701-2707.
- [19] Driouich M., Gueraoui K., Sammouda M., Haddad M.Y., A New Numerical Code to Study the Flow of Molten Polymers In Elastic Pipes. *AES-ATEMA International Conference Series - Advances and Trends in Engineering Materials and their Applications*, (2011).
- [20] Driouich M., Gueraoui K., Sammouda M., Haddad Y. M., Aberdane I, The Effect of Electric Field on the Flow of a Compressible Ionized Fluid in a Cylindrical Tube. *Adv. Studies Theor. Phys.*, Vol. 6, no. 14, (2012) 687-696
- [21] Driouich M., Gueraoui K., Sammouda M., Haddad Y.M., The Effect of the Rheological Characteristics of the Molten Polymer on its Flow in Rigid Cylindrical Tubes. *Adv. Studies Theor. Phys.*, 6(12) (2012) 569-586
- [22] M. Sammouda, K. Gueraoui, M. Driouich, A. El Hammoumi, A. Iben Brahim, Non-Darcy Natural Convection Heat Transfer along a Vertical Cylinder Filled by a Porous Media with Variable Porosity, (2012) *International Review of Mechanical Engineering (IREME)*, 6 (4), pp. 698-704.
- [23] Sammouda, M., Gueraoui, K., Driouich, M., Ghouli, A., Dhiri, A., Double Diffusive Natural Convection in Non-Darcy Porous Media with Non-Uniform Porosity, (2013) *International Review of Mechanical Engineering (IREME)*, 7 (6), pp. 1021-1030.
- [24] El Khaoudi, F., Gueraoui, K., Driouich, M., Sammouda, M., Numerical and Theoretical Modeling of Natural Convection of Nanofluids in a Vertical Rectangular Cavity, (2014) *International Review on Modelling and Simulations (IREMOS)*, 7 (2), pp. 350-355.  
<http://dx.doi.org/10.15866/iremos.v7i2.585>
- [25] Tricha, M., Gueraoui, K., Zeggwagh, G., Mzard, A., New Numerical and Theoretical Approaches to Study the Blood Flows at Microcirculation Level, (2014) *International Review of Mechanical Engineering (IREME)*, 8 (6), pp. 1043-1046.  
<http://dx.doi.org/10.15866/ireme.v8i6.2725>
- [26] H. Ezbakhe, S. Bousad, A. El Bakkour, T. Ajzoul et A. El Bouardi ; Etude Thermique de la Terre Stabilisée au Ciment Utilisée en Construction au Nord du Maroc , *Rev. Energ. Ren. : Journées de Thermique* (2001) 69-72.
- [27] Nadia benmansour, Boudjemaa Agoudjil , Abderrahim Boudenne, Etude des performances de produits renouvelables et locaux adaptés à l'isolation thermique dans le bâtiment, *XXIXe Rencontres Universitaires de Génie Civil*. Tlemcen, 29 au 31 Mai 2011.
- [28] Márcio Buson, Nuno Lopes, Humberto Varum, Rosa Maria Sposto and Paulo Vila Real, *Fire resistance of walls made of soil-cement and Kraftterra compressed earth blocks*, FIRE AND MATERIALS .Fire Mater. (2012). Published online in Wiley Online Library (wileyonlinelibrary.com). DOI: 10.1002/fam.2148.
- [29] Pierre-Antoine Chabriac , Antonin Fabbri , Jean-Claude Morel , Jean-Paul Laurent and Joachim Blanc-Gonnet, A Procedure to Measure the in-Situ Hygrothermal Behavior of Earth Walls, *Materials* 2014, 7, 3002-3020.  
doi:10.3390/ma7043002.
- [30] A Madhumathi, J.Vishnupriya, S Vignesh, Sustainability of traditional rural mud houses in Tamilnadu, India: An analysis related to thermal comfort, *Journal of Multidisciplinary Engineering Science and Technology (JMEST)* ISSN: 3159-0040 Vol. 1 Issue 5, December – 2014.
- [31] Dervilla Niall, Sarah McCormack, Philip Griffiths, Luisa Cabeza, *Thermal Energy Storage in Building Integrated Thermal Systems: A Review. Part 2. Integration as Passive System*, Engineering: Education and Innovation, Niall, D. et al. (2015) *Thermal Energy Storage in Building Integrated Thermal Systems: A Review. Part 2. Integration as Passive System*, *Journal Renewable Energy*, vol. 85, January 2016 pp. 1334-1356.

## Authors' information

<sup>1</sup>Team of Modeling and simulating in Mechanics and Energetic, Faculty of Sciences, Mohamed V University, B.P. 1014, Rabat, Morocco.

<sup>2</sup>Laboratory of Mechanics and Materials, Faculty of Sciences, Mohamed V University, B.P. 1014, Rabat, Morocco.

<sup>3</sup>Department of Mechanical Engineering, University of Ottawa, Ottawa, Canada, K1N 6N5.



**Najat Zakham** was born at Jeddah KSA, 13th October 1980. Graduated in 2000-2004 with a Bachelor (BSc) Degree in physics at Faculty of Education in Hodeida Yemen and graduated in a Master degree in 2010-2012 in physics-informatics, Faculty of science- University Mohammed V- Rabat- Morocco.

# Effect of Soil Drainage on California Bearing Ratio of Soaked Clay

Robert G. Nini<sup>1</sup>, Michel Y. Chalhoub<sup>2</sup>

---

**Abstract** – *The quality of pavement is affected mostly by the type of subgrade soil, and in many countries, the subgrade soil is clay. The California Bearing Ratio CBR of clay is generally very low which leads to a thicker layer of pavement and sub base materials. This increase in quantities leads to a significant increase in cost. Since the use of the clay as subgrade is inevitable, many private and public institutions searched on a way to increase its CBR, but most of the conducted studies focused on increasing clay CBR by reinforcing the clay either by geogrids or by fibers which are very expensive. One common finding in all the studies was that the CBR of unsoaked clay is higher than CBR of soaked one which means that CBR of clay is affected by its moisture content. In our work, the objective is to increase the CBR of clay by draining it instead of reinforcing it. Drainage can be obtained by adding a layer of granular soil between clay layers. Sand was used as granular soil for the sake of its workability in the CBR mold and for its relatively small particles size. Our aim is to verify if sandy layer can play a drainage role for the clayey soil and to also find the most efficient position of the sandy layer. We collected six soils from different regions to cover as much as possible the different clay types in Lebanon. For each soil, we found CBR values for clay alone and clay with layer of sand and compared them. Identification tests were necessary in order to build our analysis. At the end, from the results and analysis, we found the position of the sandy layer which increases most the clay CBR and we proved that the existence of sandy layer is beneficial for CBR of clay. Copyright © 2016 Praise Worthy Prize S.r.l. - All rights reserved.*

**Keywords:** *Clay, Subgrade, CBR, Sand, Drainage*

---

## I. Introduction

Clayey soils are known by their weak value of soaked California Bearing Ratio CBR. Even after placing borrowed subbase and base granular materials above the subgrade clayey soil, the clay will be subjected to settlement under traffic surcharge. Previous researches worked on clay CBR increasing by reinforcing it with geogrids [1], with artificial fibres [2], with fly ash [3] or with natural fibres [4]. Reinforcing materials are very expensive and working on the stiffness only does not solve the whole problem. The real problem of the clayey subgrade is the excess of pore water pressure trapped between clay particles. The most efficient solution is to dissipate the excess water pressure by using a drain material consisting of any granular soil. Due to the laboratory scale of our soil container which consists of cylindrical mould of 6 inches diameter, the selection of sand as granular soil will be the best choice regarding its small particles diameter. The objective of this project is to find the position of the sandy layer which will enhance most the CBR of clayey soils and to find how much it will increase CBR of clayey soil.

This research consists of two parts:

- a. Experimental part: This section deals with tests performed in soil laboratory as Proctor test [5] and CBR test [6]. The CBR test used in this work is the normal one even that new researches were made on

dynamic CBR [7]. More identification experiments will be needed to recognize the clayey soils parameters as sieve analysis [8], specific gravity [9], Atterberg limits [10] and hydrometer test [11].

- b. Analysis part: Based on the results of the experiments done on different clayey soils collected from different zones of Lebanon, the effect of the sandy layer on the CBR values of the clayey soils will be studied.

## II. Experimental Part

The working on different types of clayey soils was a necessity in order to cover as much as possible different types of Lebanese clayey soils. Dealing with clay is not a simple task because of its sticky behaviour and its high sensitivity to water [12].

Many assumptions were made in order to accomplish all the experiments. Otherwise, the project could not progress. The steps and the assumptions were exactly the same for the six soils.

### II.1. California Bearing Ratio and Proctor Tests

We collected six clayey samples from different regions of Lebanon. The six soils are extracted from Daher El Ain, Aitou, Koura, Amyoun, Ehden and Zgharta regions.

First, the Proctor test was done separately on the six soils in order to find the optimum moisture content OMC and the maximum dry density MDD which will be used to compact these soils for the CBR test. After it, the CBR test will be performed on the six clayey collected samples and will be named CBR of “Pure Clay” of each one. Then, we will repeat the CBR test on these clayey soils but this time after placing the sandy layer within the five compacted layers of soil in the mould. Fig. 1 shows the details of the soil layers. Each time, we will change the position of the sandy layer according to the followings:

*Case 1:* Compacting the clayey soil in Proctor mould including a sandy layer at bottom and four layers of clay above the sandy layer. This case was named “Bottom sandy layer”.

*Case 2:* Compacting the clayey soil in Proctor mould including at bottom a clayey layer followed by a sandy layer and three other layers of clay after the sandy one. This case was named “Second sandy layer”.

*Case 3:* Compacting the clayey soil in Proctor mould including at bottom two clayey layers followed by a sandy layer and two other layers of clay above the sandy one. This case was named “Third sandy layer”.

*Case 4:* Compacting the clayey soil in Proctor mould including at bottom three clayey layers followed by a sandy layer and other layer of clay above the sandy one.

This case was named “Upper sandy layer”.



Fig. 1. One of the position of sandy layer in Proctor mould after compaction

Once, after performing all the tests, comparison of the CBR values on all these cases will be done in order to find the optimum values.

### II.2. Identification Tests

In order to analyse the behaviour of each clayey sample and its five cases (one case of pure clay and four others cases with sandy layer at different positions), performing the identification tests is a must especially that some of the clayey parameters affect directly its CBR value [13].

As for the identification tests, we performed the following tests:

- a- Sieve analysis to get the percentage of particles passing sieve number 200,
- b- Atterberg limits in order to get the liquid limit, the plastic limit and the plasticity index.
- c- Specific gravity test was a necessity in order to finish the hydrometer calculations
- d- Hydrometer test to get the clayey fractions.

More than three hundred hours we have passed in the laboratory to finish all needed experiments which their results are presented in Table I.

TABLE I  
THE IDENTIFICATION TEST RESULTS OF THE SIX USED CLAYEY SAMPLES

	Soil 1 Daher Ain	Soil 2 Aitou	Soil 3 Koura	Soil 4 Amyoun	Soil 5 Ehden	Soil 6 Zgharta
Clay fraction %	58	39.5	51.4	41.9	42.4	50.2
Silt fraction %	19	19.5	19.6	21.1	37.6	24.8
Plasticity Index %	32.6	26.1	30.4	27.3	29.2	24.8
OMC %	19.2	17.4	18.8	18.0	13.0	14.2
MDD KN/m <sup>3</sup>	17.35	17.60	17.39	17.49	16.54	16.8

### III. Analysis of Results

After performing the CBR tests on the different clayey soils according to the five cases, we plotted all the CBR curves of each six soils according to the five cases in Fig. 2 to Fig. 7.

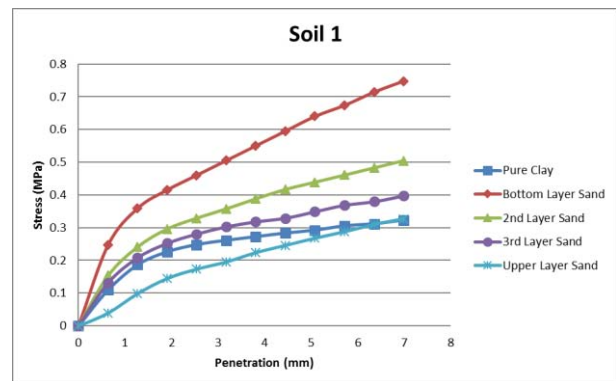


Fig. 2. Stress versus penetration of the five cases on soil 1

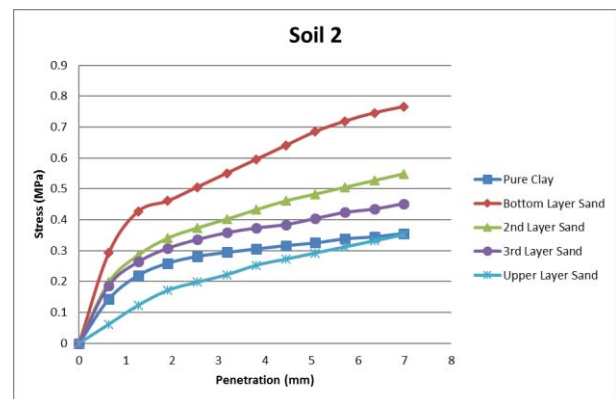


Fig. 3. Stress versus penetration of the five cases on soil 2

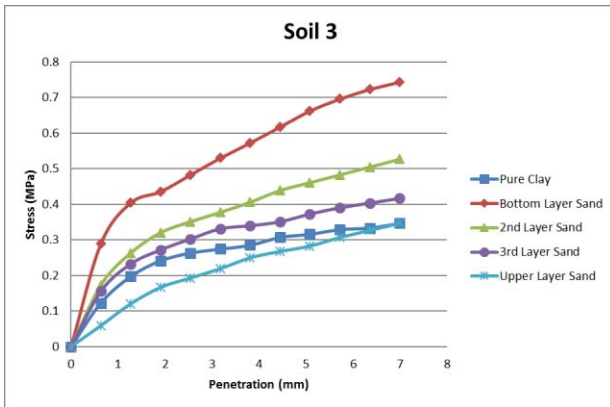


Fig. 4. Stress versus penetration of the five cases on soil 3

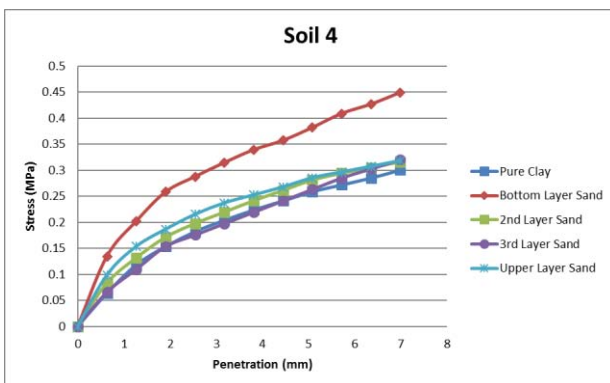


Fig. 5. Stress versus penetration of the five cases on soil 4

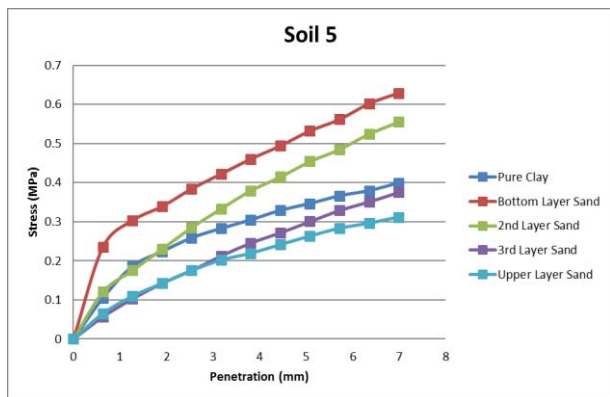


Fig. 6. Stress versus penetration of the five cases on soil 5

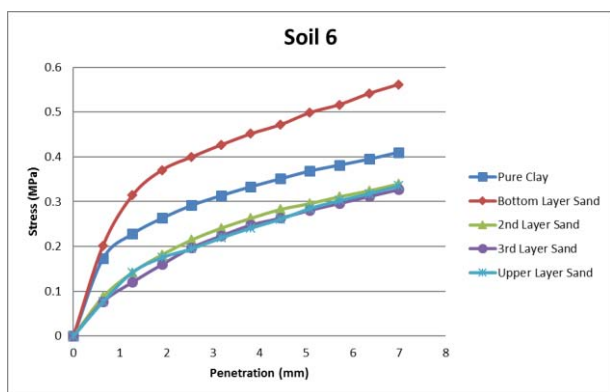


Fig. 7. Stress versus penetration of the five cases on soil 6

After analyzing all the above curves, we can give the following results:

- 1- The case of the bottom sandy layer gives the higher CBR values at 0.2 inch (5 mm) for all the soils. The CBR increasing ratio between the pure clay and the case of the clay with bottom layer of sand are respectively: 2.21, 2.16, 2.06, 1.46, 1.51 and 1.35. This CBR increasing is explained by the fact that the stress applied on soil at 0.2 inches penetration causes high excess of pore water pressure in clay. This excess of water pressure trapped in clay due to applied pressure will be easily dissipated by the sandy layer under higher pressure, this means under larger penetration. Having a sandy layer at bottom will help dissipating the clay water from all the layers above it due to gravity and excess of water pressure. Water will be squeezed out of clay through sandy layer. Draining water out from clay increases clay stiffness. The efficiency of filtering function of sand is at its maximum. When the sandy layer is located at middle of the mould, it plays a drainage line for only the upper clayey layers.
- 2- Nothing changed concerning the increasing ratio of CBR when the thickness of the sandy bottom layer was increased. This is easily explained by the fact that the filter criteria of sand govern its stiffness criteria, so whatever will be the sandy layer thickness, the increasing ratio of CBR will remains almost constant. In order to generalize this idea, further experiments should be done.
- 3- By changing the position of the sandy layer and getting it up, the stiffness criteria of sand governs its filter criteria. This means that when the sandy layer is moved up to reach the upper layer, its low stiffness contributes to reduction of clay CBR before the excess of clay water starts to drain out through it. It is known that sand stiffness could not be relatively increased by compacting it.
- 4- In the above charts, all the curves interfere at the beginning of penetration. This is explained by the fact that under low applied pressure, the drainage function of sandy layer is not activated due to the low triggered clay water pressure. While the applied pressure gets high, the sand drainage function starts working. In fact, the efficiency of the sandy layer is very clear in the case of bottom sandy layer.
- 5- The CBR increasing ratio in the case of bottom sandy layer is noticeable in soil 1,2,3 and 4, while in soil 5 and 6 this ratio relatively decreases. Soil 5 and soil 6 include silt fraction more than the other soils. The silt is known by its higher permeability than the clay. That is why the sand drainage efficiency decreases for these soils because it is less efficient with types of clay having relatively higher permeability.

#### IV. Conclusion

All the previous tests and their results demonstrated that the existence of sandy layer is beneficial for CBR

value of clayey soil. Deeper is the sandy layer in the Proctor mold, higher is the drainage of clay excess pore water and therefore obtaining larger CBR. When the position of the sandy layer is moving up close to the ground surface, its relatively weak stiffness will affect negatively the clay CBR.

Also this paper found that under higher pressure, the efficiency of sandy layer is larger than under lower pressure. Moreover, we found that it is not important the stiffness and the thickness of the filter sandy layer, what is more important are the position and the drainage capacity of the sandy layer.

## References

- [1] P. Singh and K.S. Gill, CBR improvement of clayey soil with Geo-grid reinforcement,, *International Journal of Emerging Technology and Advanced Engineering*, Vol. 2(Issue 6):456-462, 2012.
- [2] B. Soundara and K. P. Senthil Kumar, The effect of fibres on properties of clay, *International Journal of Engineering and Applied Sciences*, Vol. 2(Issue 5):110-116, 2015.
- [3] B. Singh and A. Kalita, Influence of fly ash and cement on CBR behavior of lateritic soil and sand, *International Journal of Geotechnical Engineering*, Vol. 7(Issue 2): 173-177,2013.
- [4] H. Sarbaz, H. Ghiassian and A. A. Heshmati, CBR strength of reinforced soil with natural fibres and considering environmental conditions, *International Journal of Pavement Engineering*, Vol. 15(Issue 7):557-583, 2013
- [5] ASTM Standard D698, Standard Test Methods for Laboratory Compaction Characteristics of Soil Using Standard Effort (ASTM International, 2001, pp. 78-88).
- [6] ASTM Standard D1883, Standard Test Methods for CBR of Laboratory-Compacted Soils (ASTM International, 2001, pp. 170-177).
- [7] K. Zabielska-Adamska and M.J. Sulewska, Dynamic CBR test to assess the soil compaction, *Journal of Testing and Evaluation*, Vol. 43(Issue 5):1028-1036, 2015.
- [8] ASTM Standard D422, Standard Test Methods for Particle-Size Analysis of Soils (ASTM International, 2001, pp. 10-17)
- [9] ASTM Standard D854, Standard Test Methods for Specific Gravity of Soil Solids by Water Pycnometer (ASTM International, 2001, pp. 93-99)
- [10] ASTM Standard D4318, Standard Test Methods for Liquid Limit, Plastic Limit and Plasticity Index of Soils (ASTM International, 2001, pp. 561-574)
- [11] ASTM Standard D1140, Standard Test Methods for Amount of Material in Soils Finer Than the No. 200 Sieve (ASTM International, 2001, pp. 100-103)
- [12] V. Olphen, Clay-water relationship-Theory and application, A review, *IUPAC-Conference on Colloid and Surface Science*, pp. 46-53, Budapest, 1975
- [13] S. A. Naeini and A. R. Ziaie\_Moayed, Effect of Plasticity Index and reinforcement on the CBR value of soft clay, *International Journal of Civil Engineering*, Vol. 7(Issue 2):124-130, 2009.

## Authors' information

<sup>1</sup>University of Balamand, civil engineering department, Lebanon.

<sup>2</sup>Université of Saint Esprit de Kaslik, civil engineering department, lebanon.



**Robert Nini** is born in Tripoli, Lebanon at 1970. He had his PhD in Geotechnical Engineering from Ecole Centrale de Paris, France in 2004. He is an associate professor at University of Balamand, Lebanon. He is working currently on CBR of the Lebanese clay. He contributed in many conference papers on

Analysis of factors causing slope instabilities, landslide hazard mapping, plasticity of clay and CBR of clay under cyclic load. Dr. Nini is a member of Order of Engineers and Architects, Lebanon.



**Michel Chalhoub** is an associate professor of structures at the "Université of Saint Esprit de Kaslik, Lebanon" A specialist of historical monuments retrofitting, he is the owner and the director of Distruct solutions for engineering and construction. His research activities cover the numerical modeling of fractured rock masses and masonry structures. Dr.Chalhoub is a member of Order of Engineers and Architects, Lebanon.

# Relationship between Bituminous Mastic and Mix Asphalt Properties

Wahib Youssef, Abidi My Larbi

---

**Abstract** – The bituminous mastic consists of fine elements (whose diameter is less than 80 $\mu$ m) resulting from the mineral mixture of the mix asphalt and the asphalt itself, whose amount is fixed by the mixture formulation. Due to its composition that results from the asphalt mix, the bituminous mastic constitutes the structure and the effective joining that connects the different mix constituents and also ensures the filling of the voids existing in the mix; its characteristics influence the properties of the asphalt mix to more resist to the heavy loads traffics during useful life of road. Thus, there are determining relations between the bituminous mastic and the performances of the mix asphalt, such as the mechanical resistance to heavy loads, rutting and water holding. **Copyright** © 2016 Praise Worthy Prize S.r.l. - All rights reserved.

**Keywords:** Aggregates, Asphalt, Bituminous Mastic, Mix, Module of Rigidity, Rutting, Voids

---

## I. Introduction

Nowadays, the road is considered one of the main infrastructures, due to its important mission, in insuring the transportation of different goods from a region to another; in this sense, the roadway must show its ability to resist to intensive weights. For this reason, a particular attention should be paid to the mechanical performances of asphalt mix that constitutes the roads.

In order to better understand the behavior of the mix asphalt, it is essential to take the bituminous mastic as a model, in view of its importance in the connection of the various elements constituting the mix asphalt [1].

Thus, the mastic, constituted by fines and bitumen, becomes the principal binder of the mix. The bitumen amount and the quantity of fines remain important in the mix asphalt; indeed, the bitumen binder naturally transmits its viscous-elastic behavior to the mix asphalt whereas the fines ensure the cohesion and the stability of mixture [2]. It is thus necessary to define an optimal dosage of asphalt in order to ensure the cohesion of the mixture as well as the good coating of all the mixture's aggregates by the bitumen, and this, while avoiding the problems of rutting at high temperature.

## II. Relationship between Mechanical Performance of Mix and the Contact Aggregate-Asphalt

The mechanical performances of the mix asphalt are depending on the formulation, the fabrication process, the materials used, and especially the nature of the contact between asphalt and the aggregates (affinity).

This contact could be studied on the service condition (ambient temperature) or during the manufacturing phase. On service conditions, the study of the quality of mix asphalt can be carried out on several levels:

- On the interface of the asphalt-aggregate.
- On the asphalt mix (test of water holding).

### II.1. Interface of Asphalt-Aggregate

#### a- Impact of the Aggregates Characteristics

The aggregates don't have the same affinity with asphalt. Curtis et al. (1993) [3] have demonstrated the impact of the chemical nature of the aggregate from the absorption measurements of asphalt on many aggregates surfaces.

They have concluded that the calcareous aggregates have a better affinity than the siliceous ones.

The aggregates from the mechanical crushing of solid rocks have better affinity in comparison with those resulting from materials with rounded facets.

#### b- Impact of Asphalt's Characteristics

Asphalt is a mixture of hydrocarbons, mainly the aliphatic ones, but it contains some polar and organometallic ingredients like nickel, vanadium, and iron. According to Plancher et al. (1997) [4], the ingredients of asphalt that have more affinity with the aggregates are in the following order: the carboxylic acids, the anhydride, the quinolones, the sulfoxydes, and the ketones.

However, these ingredients that adhere to the aggregate's surface experience a loss of bond between the asphalt binder and the aggregate, when water is present. The active adhesion (adhesion including water) of asphalt varies inversely to its viscosity (Ramond, on 1977) [5].

#### c- Contact Angle of Aggregate-Asphalt

Mechanical interactions occur on the interface of asphalt and aggregates, and they arise from a more or less close interpenetrating of materials.

This connection is due, on the microscopic scale, to the geometric structures. The adhesivity results from the affinity between the asphalt molecules and the ones of the aggregate. This affinity result from the tendency of the fluid to spread on the solid's surface to create a coating; this incites us to consider the contact angle of the two, in order to allow us to evaluate the capacity of the binder to wet/coat the surface of the aggregate [6].

The general experiment of this contact angle is studied using a drop of asphalt on the surface of aggregate, and by identifying the angle  $\theta$  (Fig. 1 below) formed by the drop and the surface. The more the angle decreases, the more the affinity between the drop and the surface increases [7].

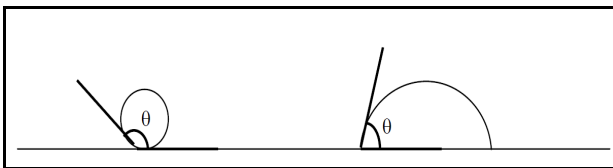


Fig. 1. Contact angle between the drop and the surface

The existence of small elements ( $\leq 80\mu\text{m}$ ) improves the affinity between aggregate and asphalt, by reducing the contact angle.

### III. Factors Influencing Bituminous Mastics Well as the Mix Asphalt

Since the components of the mastic which are the same of the mix asphalt, the formulation method of the latter determines the properties of the mastic.

Then, the nature and the amounts of aggregates and asphalt fixed by the formulation are in relation to the bituminous mastic.

#### III.1. Types of Mineral Structure of the Asphalt Mixture

The composition of mix asphalt as a mixture leads us to distinguish three families of the mixture [8], which are:

- The stone structure;
- The sand structure;
- The filler structure.

##### - Mixture with the stone structure:

this kind of mixture is characterized by a high amount of stone (at least 70% of the mineral mixture); this type of mixture generates a high percentage of the voids (over 20%), so it is often used in the draining mix asphalt.

##### - Mixture with sand structure:

the sand really constitutes the structure of the mix asphalt considering its high percentage in the mixture (more than 60%). In fact, the characteristics of the mix depend, in this case, on the stacking of the sand elements as well as their internal friction.

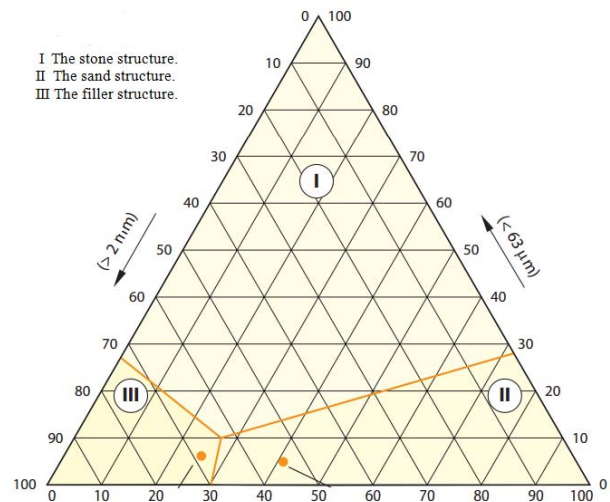


Fig. 2. Types of mineral structure

It is thus necessary to carry out an optimum stacking of the sand elements, creating a volume of the voids that allows the incorporation of an adequate volume of mastic, ensuring the coating without dislocating the structure.

##### - Mixture with structure of filler:

They are very firm mixtures, formed essentially by the filler's fraction, which are considered as mastics; they are often used in the treatment of the roadway cracks.

#### III.2. Method of Filling of the Mix Asphalt Voids by Bituminous Mastic

The adequate filling of the voids by bituminous mastic must comply with two conditions:

- It must be limited by a higher value in order to avoid an over-filling, which generates the risk of instability for the mix asphalt.
- The sufficient coating of the mineral mixture by bituminous mastic, to ensure the cohesion of the mixture, and this requires an optimal dosage rate of asphalt.

##### a- Determination of the Volume of Vacuum Available in Mastic

Considering the composition of mastic, its volume is the sum of two volumes: the one of fines added to the volume of asphalt. The volume of mastic cannot exceed the volume of the voids of the mineral structure of mix asphalt. So, it is recommended that the mastic partially fill the volume of voids so as to afford a free volume for giving the mix asphalt a minimal volume of voids.

The maximum volume available for the mastic is obtained by deducing the percentage of the voids of the mineral mixture, (the minimal value desired in the mix asphalt) [9].

It is necessary to check if obtained volume, is sufficient to contain mastic, if not, it is to re-examine the aggregate size of the mixture by modifying the

formulation (percentage of the components of mix) or to change the components (Aggregate and sand).

*b- Role of the Voids in the Mix Asphalt*

In mix asphalt, the presence of voids is essential to take account the expansion phenomena related to the specific properties of the bitumen (thermal expansion). However, some researchers have put into perspective the beneficial role for the mix voids on the resistance to rutting.

*III.3. Composition of the Mastic: Relationship Between the Percentage of Fines and Bitumen Dosage*

After having estimated the volume of the mastic to be incorporated in the mixture, it will be time to determine its composition. This mastic must have a consistency and a thermal susceptibility that will bestow on the mixture cohesion and stability that are both depended to the conditions of use.

A simple method based on the code of good practice of the Highway Research Centre CRR R 69/97- in Brussels, makes possible to check the composition of mastic [10].

According to this method, the main factors influencing the mastic properties are:

- The characteristic of the bitumen (especially: penetrability, softening, and viscosity).
- The stiffening ability of fines, that depends on the nature on the fines and their characteristics and especially the index of the voids RIGDEN that determines the percentage of fines voids.
- The ratio (K) of volumes between that of fines and the one of bitumen.

The Fig. 3 below, resulting from a statistical analysis, represents the increase in the temperature of softening Ball and Ring tests according to the report K and of volume  $V_F$  (volume voids of fines).

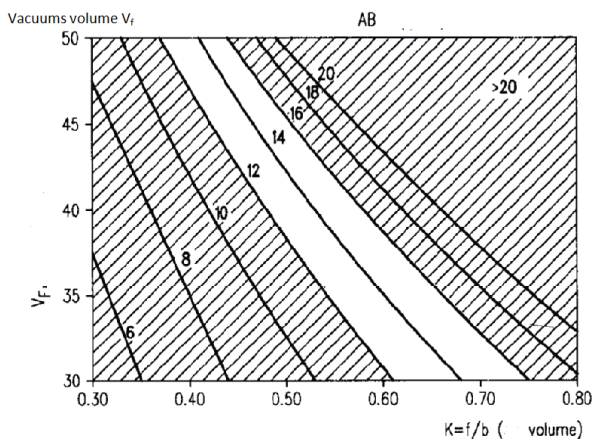


Fig. 3. Relationship between the stiffening power, report K and  $V_f$

It is necessary to satisfy, for the fines, a higher volume  $V_F$  of the voids, which means high stiffening ability, and

a low value of K. The fines with a low  $V_F$  are combined with a high value of K.

**IV. Bituminous Mastic and Mix Asphalt Properties**

*IV.1. The Bituminous Mastic and Resistance to Rutting*

*a- Percentage of the Voids and Rutting*

The interstitial voids play a significant role in resistance to the rutting of mix asphalts. The decrease of the air content in a mix asphalt increases its durability as well as its resistances to rutting [11]. These voids are specified in the practical case by the compactness of the mix asphalt using the gyratory shear compactor; indeed the percentage of the voids is equal the difference of 100 minus compactness rate (in %). The higher the compactness of the mix asphalt is, the more the rutting resistance increases. This is demonstrated according to the experiment carried out by Proteau and Paquin [12], the results are given in the Fig. 4 below.

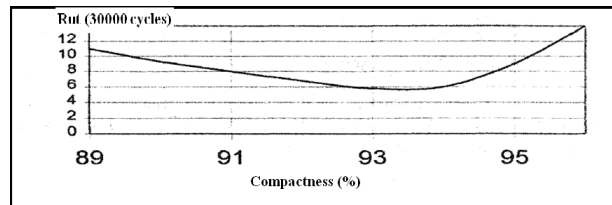


Fig. 4. Influence of compactness on the rutting resistance

According to the graph, we notice the reduction of rut-depth with the increase in the mix asphalt compactness, up to an optimal value corresponding to compactness close to 93.7%. The increase in compactness is explained by the decrease in volumes of the voids of the mix asphalt, which increases its rigidity and improves the rutting resistance.

*b- The Influence of Both: the Type of the Mineral Structure and the Bitumen Grade on the Mix Rutting*

The nature and the type of the mineral mixture define the mix asphalt behavior; indeed a sandy mixture is more sensitive to rutting, also the shape of the aggregates (the round shapes give bad results of rutting) and this is well illustrated in the Fig. 5, according to an experiment carried out by Belgian research centre CRR [13]. We conclude that, the use of angular materials improves more the resistance to rutting. The bitumen grade influences the resistance to rutting; indeed, rigid bitumen gives a more important resistance than a soft one [14], this is illustrated in the Figure 6, according to an experiment carried out by Belgian research centre CRR.

*IV.2. Bituminous Mastic and the Mix Asphalt Water Holding*

The water holding capacity of the mix asphalt depends on the formulation (mainly, the resulting volume of

voids), the nature of the aggregates and the bitumen, and the most important factor is the contact between the two, the effective bonding agent that connects them: the bituminous mastic [15].

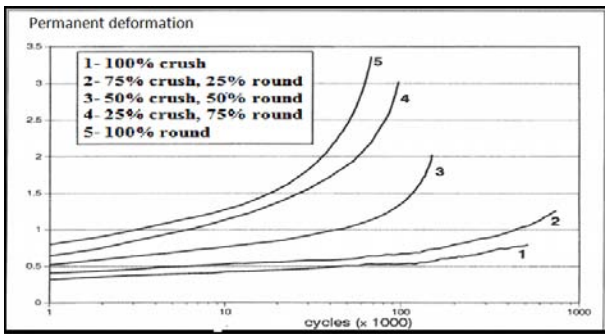


Fig. 5. Variation of rutting deformation according to the angular nature of the crushed sand

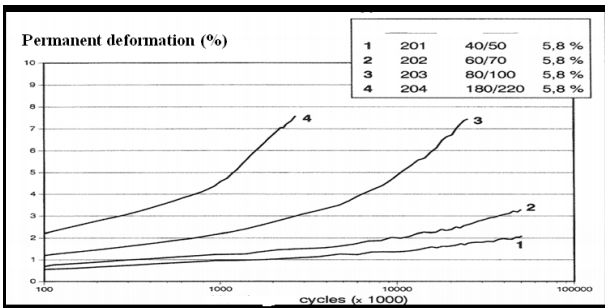


Fig. 6. Influence of the bitumen rigidity on the rutting

Considering its role in the filling of the mix asphalt voids, bituminous mastic ensures a good cohesion of the mixture, this provides a better mix asphalt compactness, which improves its waterproofing and decreases the possibility of water penetration. In this sense, we carried out a comparative study of mix asphalt (0/10mm), in which, the role of the mastic in the improvement of compactness and the water holding capacity of the mix asphalt, is revealed, using Duriez test.

The bitumen dosages are selected by respecting the limits of the usual use (because going beyond these limits leads to an overdose or under-dosage of the bitumen which generates a diminution of mechanical performance). So, we selected dosages varying from 5.6 to 6%. The results obtained are presented in the following Fig. 7. According to the graph, we notice an increase in the mix asphalt water holding behavior, according to the amount of bitumen, this is explained by the fact, that, the increase in the volume of the bituminous mastic that ensures the connection of the components and ensures the waterproofing of the mix asphalt, from which result the good water holding.

Also, we have studied the variation, of the mix compactness, with asphalt dosage. So, we selected dosages rates varying from 5.6 to 6%. The results obtained are presented in the Fig. 8.

According to the graph, we notice an increase of mix compactness, with the increase of amount of asphalt.

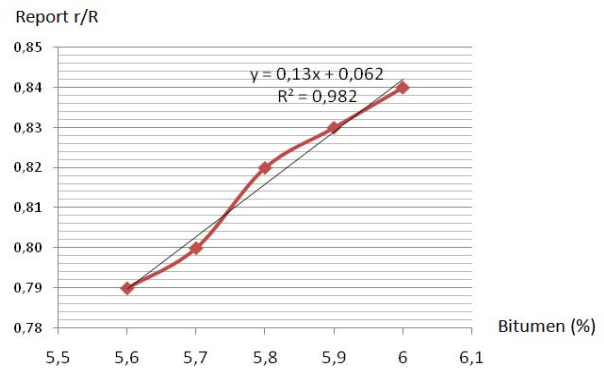


Fig. 7. Influence of bitumen dosage rate on the mix asphalt water holding behavior

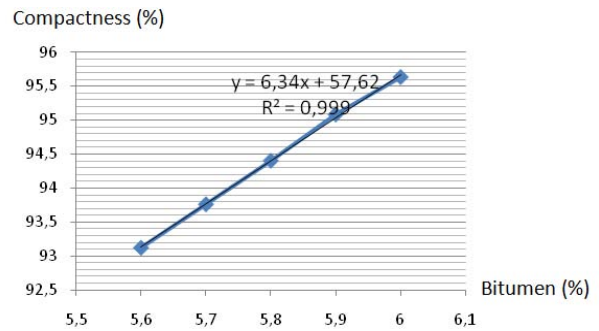


Fig. 8. Influence of bitumen dosage rate on the compactness of mix asphalt

This is explained by the fact that, the increase of bitumen dosage rate, contributes to the increase in the volume of the bituminous mastic that ensures the connection of the components, and reduces the volume of voids of mix asphalt.

Moreover, we have proceeded to carry out another experiment, which consists in determining the influence of the quality of fines on the water holding behavior of the mix asphalt, for this purpose, we have chosen in the formulation of mix asphalt two sands of different characteristics.

The identification results of two sands as well as the corresponding stiffening powers of bituminous mastics and the water holding behavior are given in the following Table I. The stiffening ability of sand 1, is more important than the one of sand 2, this is explained by the fact that, the cleanliness of sand 1 as well as the nature of fines that are better than those of sand 2.

TABLE I  
CHARACTERISTICS OF SANDS USED AND THEIR STIFFENING POWER AND WATER HOLDING BEHAVIOR OF RESULTING MIX

Tests	Sand 1	Sand 2
Equivalent sand %	76	63
Percentage of fines (<80µm)	08	10
Stiffening ability of mastic	12	09
Water holding (bitumen: 5.8%)	0.86	0.82

These parameters influence the contact between the bitumen and the fines, which explain the variation of the stiffening power.

This stiffening of bituminous mastic ensures the good connection of the components of mix asphalt, which decreases the volume of the voids and increases the waterproofness, from which results the good water holding of mix asphalt.

IV.3. Bituminous Mastic and Mix Module of Rigidity

The module of rigidity of mix asphalt is an important parameter, which acts on the behavior of the bituminous mixture, it depends on several parameters, and the most important are the components of mix: the aggregates and asphalt.

Indeed, the quality of asphalt, its rigidity and its thermal susceptibility, influences the module of rigidity, an asphalt with high rigidity, confer on the mix, a better module of rigidity; also the composition and the nature of constituents and the volume of the voids, are important parameters to determine the module of rigidity.

The bituminous mastic constitute the mainly binder of the mix, because it assures the connection between the various constituents and assures the filling of the voids, and seen its composition (asphalt and fines), its properties are related to those of the module of rigidity of mix. A study is doing by the Canadian laboratory of road [16], to determine the relation between asphalt and the module of mix asphalt, and for this, five typifies of asphalt most used are tested; the used asphalts are : PG 58-28, PG 58-34, PG 64-28, PG 64-34 and PG 70-28.

The term "PG H-L" means "Performance Rank High-Low". The letter "H" corresponds to the high temperature and the letter "L" corresponds to the minimal temperature, the characteristics of used asphalts are given in the following Table I.

TABLE II  
CHARACTERISTICS OF ASPHALTS USED IN THE STUDY

Tests	PG58-28	PG58-34	PG64-28	PG64-34	PG70-28
Temperature max (°C)	59.7	60.8	65.2	64.1	71.8
Temperature min (°C)	-28.6	-34.3	-29.3	-32.4	-30.5
Temperature ball ring (°C)	46.4	43.6	49.9	59.2	58.1

a- Influence of asphalt grade on mix module of rigidity

The test consists of measurement of mix module (the frequency is 10Hz) for different asphalts grade, the results is given in Fig. 9 below.

The results show that the type of asphalt influences the module of rigidity of the mix asphalt, and this influence increases with the temperature. The module of mix varies from 7 200 to 11 500 MPa (in 10°C and 10Hz) according to the type of used asphalt.

The results shows that the module of rigidity |E\*| with an asphalt PG H-28 is generally higher in intermediate temperature (10 °C) than that of the mix asphalt with an asphalt PG H-34.

The grade of asphalt also influences the module of rigidity at high temperature (> 40 °C), the mix asphalt with an asphalt PG 70-L has a module of rigidity higher

than the one with an asphalt PG 64-L, which have a higher module than the mix asphalt with an asphalt PG 58-L. According to these results, we conclude the influence asphalt grade (for the same temperature) on the module of rigidity of mix asphalt.

b- Influence of voids on module of rigidity

The parameters which influence the module of the mix are the asphalt grade, the frequency and the temperature.

Another study from the Canadian laboratory, demonstrates that the voids of the mix influence the module of rigidity |E\*|.

The Fig. 10 shows the influence of the voids on the module of rigidity (in 10 °C and 10 Hz) of mix asphalt with an asphalt PG 58 34.

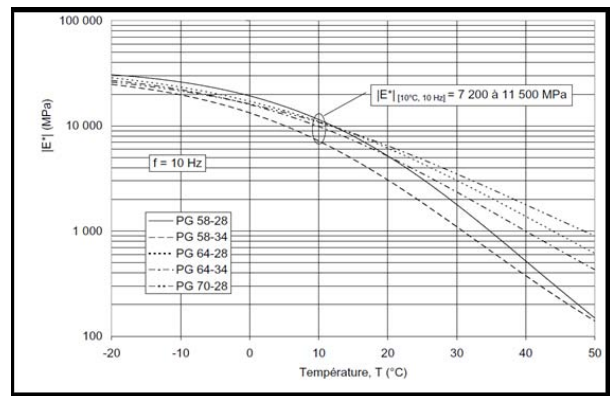


Fig. 9. Influence of asphalt grade on mix module of rigidity

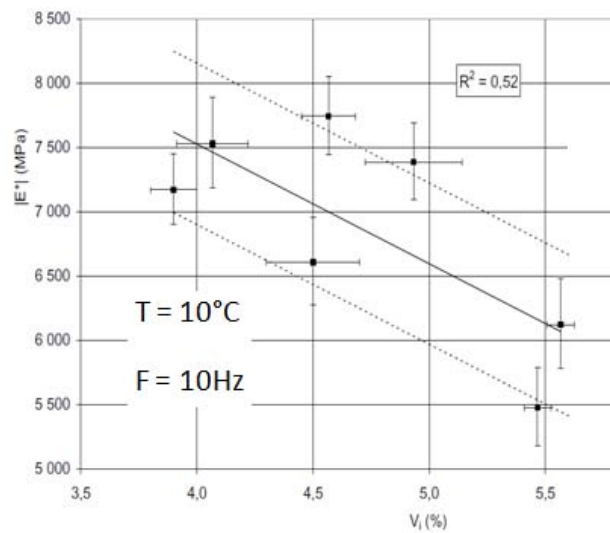


Fig. 10. Influence of voids (V<sub>v</sub>) on module of rigidity

We notice a decrease of the module of rigidity with the increase of the voids, the module of rigidity vary from 7500 MPa to 6100 MPa, when the voids varies from 4 to 5.5%. The module of rigidity decreases 930 MPa when the voids vary with 1 %.

We conclude that, the volume of voids in mix asphalt is depending of the module of rigidity: that, less the voids are, more the compactness of mix increase, which

contribute to ameliorate the module of rigidity.

According to all these results, we conclude that the module of rigidity depends on two parameters, the asphalt grade and the volume of voids.

Because the mastic constitutes the binder connecting the constituents of mix, thus it constitutes an important element in the determination of volume of voids, also the asphalt grade allows to determine the rigidity of the mastic, and we have already seen, that these two parameters influence the module of mix, from where we conclude the role of mastic in the amelioration of the module of mix asphalt.

## V. Conclusion

The bituminous mastic plays a significant role in the connection of the components of mix asphalt, and it ensures the filling of the existing voids and the cohesion of the mix asphalt, this, affects the improvement of the mechanical performances of mix asphalt.

Therefore the quality, the composition and the performances of the mastic, are crucial factors for the prediction of the mix asphalt performances, in order to ameliorate the properties and to ensure the good quality of mix asphalt constituting the roadway, which positively influences the service life.

## References

- [1] Manthos, E., Performance of Asphalt Concrete Mixtures with Conventional Bitumen, (2014) *International Review of Civil Engineering (IRECE)*, 5 (5), pp. 171-175.
- [2] Glaoui, B., Merbouh, M., Bendjima, M., Van de Ven, M., Impact of Freeze-Thaw Cycles on the Performance of Polymer Modified Bitumen, (2014) *International Review of Civil Engineering (IRECE)*, 5 (4), pp. 130-134.
- [3] C. Curtis, K. Ensley, and J. Epps. Including adhesion and absorption. Strategic highway research program, National Research Council, Washington, 1993
- [4] H. Plancher, E. L. Green and J. C. Petersen, Reduction of oxidative hardening of asphalts by treatment with hydrated lime – a mechanistic study, *Proc. Association Asphalt Paving Technologists* 45, pp.1-24, 1976
- [5] G. Ramond. Adhesivity static and dynamic aspects. Technical Report Number V, LCPC, Paris, December 1977.
- [6] Information on <http://www.bitumequebec.ca/affinity-bitumen-aggregate-a.-kucharek.pdf>.
- [7] Information on <http://www.bitumequebec.ca/didier-lesueur.pdf>
- [8] Dang-Truc Nguyen, 'Prediction of the permanent deformations of the bituminous roads ', Thesis specialty structures and materials, (2007) 28-29.
- [9] Daniel Perraton, 'Rheological properties and resistance the thermal fissuring and rutting of the mix with stony', *J. Polysci. Public.*, Laval Québec, November (2007) 169.
- [10] Olard, F., Di Benedetto, H., Vaniscote, J.C., Eckmann, B., "Failure behavior of bituminous binders and mixes at low temperatures", *Paper submitted for presentation and publication to the 3rd E&E. Congress*, Vienne, mai (2004) 12-14.
- [11] Magazine industry of roads: asphalt rutting, Vol n°8, N°3, October (2013) 10.
- [12] Saoula S., 'Modeling Approach and Valuation of mix asphalt Modified by Addition of Polymers '.Report of Doctorate University of the Sciences and the Technology Houari Boumediene, Alger, Algeria, (2013) 165.
- [13] A.Valenstrate, ' Performances of the mix asphalt with high recycling rate ', Center of Road Research, Belgium , (2006).

- [14] Haddock, J., Pan, C., Feng, A., White, T.D. 'Effect of gradation on asphalt mixture performance', *J. TRR board #1681*, (2012) 59-68.
- [15] Di Benedetto, Hervé, Chantal De La Roche et Jean-Michel Piau (2005). «Chapter 2. Mechanical properties and thermomechanical of the bituminous mixtures », bituminous road Materials 2, Lavoisier, Paris, France, p. 75-235
- [16] Félix Doucet, Determination of the mix module, Ministry of Transport of Quebec, May 2010.

## Authors' information

Ecole Mohammadia d'ingénieurs, University Mohamed 5, Morocco.



**Wahib Youssef**, born in Fez Morocco, at 12/06/1985, Phd student in civil engineering, school Mohammadia of engineers, University Mohamed 5, Rabat, Morocco. My research is interesting about the relationship between mastic and mix asphalt properties with addition of lime.



**My. Larbi Abidi**, Phd Professor in civil engineering (Section : Materiels), and director of school Mohammadia of engineers, University Mohamed 5, Rabat, Morocco. My research is interesting about the relationship between mastic and mix asphalt properties with addition of lime.

# A Nonlinear Control Method for Autonomous Navigation Guidance

G. Carloni<sup>1</sup>, K. Bousson<sup>2</sup>

---

**Abstract** – This paper deals with a nonlinear feedback control method based on Lie derivatives for the navigation guidance of unmanned aerial vehicles (UAVs). The paper proposes a modelling concept for planar and three-dimensional navigation together with proven algorithms to cope with the autonomous navigation along waypoints and on loiters. The steps that were performed in order to validate the autonomous navigation method are clearly described. The method was successfully validated on various realistic navigation scenarios for unmanned aircraft. **Copyright** © 2016 Praise Worthy Prize S.r.l. - All rights reserved.

**Keywords:** Navigation Guidance, UAV, Nonlinear Control, Lie Derivatives, Waypoints, Loiters

---

## Nomenclature

2D	Two Dimensions
3D	Three Dimensions
$\alpha$	Stepsize
$e$	Error
$g$	Gravity Acceleration
$\gamma$	Flight Path Angle
$h$	Time-step
$h_u$	Control Gain
$J$	Performance Index
$L_{(\bullet)}$	Lie Derivative with respect to a variable ( $\bullet$ )
$q$	Reference Trajectory
$Q, Q_1, Q_2$	State Weight Matrices
$R, R_1, R_2$	Control Weight Matrices
STANAG	NATO Standardization Agreement
$\sigma$	Bank Angle
$u$	System Control Vector
UAV	Unmanned Aerial Vehicle
$V$	Aircraft Speed
$x$	System State Vector
$x$	Cartesian Coordinate ( <i>easily understandable by the context</i> )
$y$	Cartesian Coordinate
$\psi$	Heading Angle
$z$	Altitude (Vertical Cartesian Coordinate)

## I. Introduction

The use of Unmanned Aerial Vehicles (UAVs) for military as well as civilian applications has increased significantly during the last decade. Recent progresses in guidance technologies based on global positioning systems are being exploited to enable UAVs to execute mission tasks without any human interface. Various methods to design nonlinear controllers have been developed up-to-date. The main trend was developing controllers using linear quadratic regulation approach [1] and the dynamic feedback linearization method [2].

Meanwhile, the basement of flight automation for any unmanned aerial vehicle is the navigation guidance module. Navigation guidance consists in providing references (for instance, velocity, heading and flight path angle) to the control module so as to generate a flight trajectory passing through a specified sequence of given waypoints coming from a waypoint database or sequentially provided by an operator.

For surveillance matters or for some other specific tasks, the vehicle may be guided to follow a specified reference curve be it a loiter navigation or any other continuous reference trajectory.

Generally, a manned aircraft is designed for a specific mission. A common mission for transportation is usually divided in different phases like take off, climb, cruise, approach and landing. A UAV is normally designed for alternative missions. Phases of the flight, such as climbs or loiters, are previously planned and each one of them is defined by a particular path to respect constraints and specifications imposed by the authorities, the operators and/or by the designers. Usually a specific automatic flight controller is designed for a particular phase of the flight.

Waypoint navigation is mostly encountered in manned aerial vehicles missions. In case of unmanned aerial vehicle flight, pure waypoint navigation occurs only on a relatively small portion of the mission. Assume that such a vehicle has been assigned a surveillance task over an area, for instance, in case of wild fire monitoring and costal or border surveillance, or even in case of area imagery. In these situations, the trajectory of the vehicle should follow a specified pattern, that may differ from a mere point-to-point (waypoint) navigation track.

Meanwhile, whatever complicated a reference trajectory may be, it can always be sampled into a sequence of waypoints. In case of a loiter navigation at constant flight altitude, it is possible to restrict the dynamic model to two dimensions, since loiter generally occurs at constant altitude.

Current methods dealing with navigation guidance are either based on the proportional navigation concept that is borrowed from missile guidance principles [3]-[5], or on path planning method [6] inspired by robot navigation.

These methods are either well-suited for planar navigation, or requires adjustment of independent parameters in the case of three-dimensional navigation.

Besides, they may require some amount of time for signal processing (in the case of proportional navigation) that some low cost UAVs cannot afford. Furthermore, the generated navigation trajectory may undergo overshoot in case of relatively stiff turn at waypoints.

The present paper rather resorts to a systematic approach to generate navigation guidance trajectories based on a nonlinear control method elaborated by Lu and Khan [7], [8] for a reference continuous system.

That method consists in applying Lie derivatives to perform the local approximation of the system model according to its relative degree, then the control is computed as the minimizer of a quadratic cost function expressing a reference trajectory tracking error.

In this approach, the time-step related to the time sampling is kept constant. The contribution of our work is twofold: the first is to extend the method described in [7] and [8] to be able to deal with adaptive time-steps so that the local error of the reference trajectory tracking be effectively minimized on-line, and the second is to validate the extended method on waypoint and loiter navigation for UAV missions.

The paper is organized as follows: section 2 describes the nonlinear control method that will be used in further sections, it first summarizes the method developed by Lu and Khan [7], [8], then proposes an extension to it; section 3 deals with the planar navigation; section 4 copes with the three-dimensional navigation; section 5 discusses about the results of the simulations, and section 6 concludes the paper.

## II. Nonlinear Control

We first summarize in this section the aforementioned nonlinear predictive control method devised by Lu and Khan [7], [8], then we propose an extension to it so that it may account for adaptive time-step.

The method assumes that the model of the system is affine in the control, that is as in (1):

$$\dot{x} = f(x) + G(x)u \quad (1)$$

However, this equation is assumed to be on the following form where the state vector is split into two subvectors  $x_1$  and  $x_2$ :

$$\left. \begin{aligned} \dot{x}_1 &= f_1(x) \\ \dot{x}_2 &= f_2(x) + B_2(x)u \end{aligned} \right\} \quad (2)$$

with:

$$x = [x_1 \ x_2]^T$$

and consequently:

$$G = \begin{pmatrix} 0 \\ B_2 \end{pmatrix}$$

$B_2$  and  $G$  being matrices of appropriate dimensions.

The first state vector  $x_1$  in Eq. (2) is not directly dependent on the control vector. The second state vector  $x_2$ , instead, is composed of that set of differential equations that involves the control vector.

### II.1. Lu and Khan's Nonlinear Control Method

Consider the equation (2) above. Then, the relative degree  $r_i$  of state vector  $x_i(t)$ , ( $i = 1$  or  $2$ ), is defined in [2] as the minimum number of times one has to differentiate  $x_i(t)$  in order to have the control vector  $u$  appearing explicitly in the expression of  $x_i(t)$ . Let  $r_i$  be the relative degree of state vector  $x_i(t)$ , for  $i = 1$  or  $2$ . If  $h$  is the time-step, then, it is possible to approximate the state at time  $t + h$  as:

$$\begin{aligned} x_1(t+h) &\approx x_1(t) + hf_1(x) + \frac{h^2}{2!} \frac{\partial f_1(x)}{\partial x} f(x) + \dots + \\ &+ \frac{h^{r_1-1}}{r_1!} \frac{\partial^{r_1-1} f_1(x)}{\partial x^{r_1-1}} f(x) \end{aligned} \quad (3)$$

$$\begin{aligned} x_2(t+h) &\approx x_2(t) + hf_2(x) + \frac{h^2}{2!} \frac{\partial f_2(x)}{\partial x} f(x) + \dots + \\ &+ \frac{h^{r_2-1}}{r_2!} \frac{\partial^{r_2-1} f_2(x)}{\partial x^{r_2-1}} f(x) + \\ &+ \Lambda(h)W(x(t))u(t) \end{aligned} \quad (4)$$

where  $\Lambda \in \mathfrak{R}^{n \times n}$  is a diagonal matrix ( $n$  being the dimension of the state space) with elements  $\lambda_{ii}$  on the main diagonal given by:

$$\lambda_{ii}(h) = \frac{h^{r_i}}{r_i!}, \quad i = 1, \dots, n \quad (5)$$

and  $W \in \mathfrak{R}^{n \times m}$  is a matrix whose row  $i$  is defined as:

$$\begin{aligned} w_i &= \left\{ L_{g_j} \left[ L_f^{r_i-1}(x_i) \right], \dots, L_{g_m} \left[ L_f^{r_i-1}(x_i) \right] \right\} \\ i &= 1, \dots, n \end{aligned} \quad (6)$$

where vector functions  $g_1, \dots, g_m$  are the columns of matrix  $G$ , and the Lie derivative with respect to each  $g_j$  is defined as:

$$L_{g_j} \left[ L_f^{r_i-1}(x_i) \right] = \frac{\partial L_f^{r_i-1}(x_i)}{\partial x} g_j \quad (7)$$

Assuming the reference trajectory as a continuous time-function  $q(t) = [q_1(t) q_2(t)]^T$ , it is possible to define the related dynamic system as:

$$\left. \begin{aligned} \dot{q}_1 &= f_1(q) \\ \dot{q}_2 &= f_2(q) + B_2(q)u_{ref} \end{aligned} \right\} \quad (8)$$

where  $u_{ref}$  is the control reference. The reference function (representing, for instance, a nominal trajectory) can be recursively approximated as:

$$q(t+h) \approx q(t) + h\dot{q}(t) + \frac{h^2}{2!}\ddot{q}(t) + \dots + \frac{h^{r_i}}{r_i!}q^{(r_i)}(t) \quad (9)$$

The error between the actual state of the system and the reference is:

$$e(t) = x(t) - q(t) \quad (10)$$

The performance index to be considered is defined as:

$$J(u(t)) = \frac{1}{2}e^T(t)Qe(t) + \frac{1}{2}u^T(t)Ru(t) \quad (11)$$

where  $Q \in \mathfrak{R}^{n \times n}$  and  $R \in \mathfrak{R}^{m \times m}$  are at least positive semi-definite and defined by the designer.

This performance index expresses the tracking error and the control effort. In particular  $Q$  and  $R$  will be defined as:

$$Q = \begin{bmatrix} Q_1 & 0 \\ 0 & hQ_2 \end{bmatrix}, \quad R = \begin{bmatrix} 0 & 0 \\ 0 & R_2 \end{bmatrix} \quad (12)$$

The optimal predictive control for the minimized performance index is found by solving the equation  $\partial J / \partial u = 0$  for the control  $u$ . This gives:

$$u(t) = - \left\{ \left[ \Lambda(h)W(x) \right]^T Q \Lambda(h)W(x) + R \right\}^{-1} \left\{ \left[ \Lambda(h)W(x) \right]^T Q [e(t) + \dot{e}(t)] \right\} \quad (13)$$

Hence, for the system previously described, the expression of the optimizing control is given as:

$$u(t) = -P^{-1} \left\{ \begin{aligned} & \frac{1}{2h^2} \left( \frac{\partial f_1(x)}{\partial x_1} B_2 \right)^T \cdot \\ & \sqrt{b^2 - 4ac} Q_1 \left( e_1 + h\dot{e}_1 + \frac{h^2}{2!}\ddot{e}_1 \right) + \\ & + \frac{1}{h} B_2^T Q_2 (e_2 + h\dot{e}_2) \end{aligned} \right\} \quad (14)$$

where  $e_1 = x_1 - q_1$ ,  $e_2 = x_2 - q_2$ , and:

$$P = \frac{1}{4} \left( \frac{\partial f_1(x)}{\partial x_2} B_2 \right)^T Q_1 \left( \frac{\partial f_1(x)}{\partial x_2} B_2 \right) + B_2^T Q_2 B_2 + h^{-4} R_2 \quad (15)$$

## II.2. Dealing with Adaptive Time-Step

The model exposed above may either be used with a constant value of the time-step  $h$  (which, as proved in [7], may be seen as the controller gain), or with an optimization procedure that computes a value of the time-step that minimizes the cost function in (11) assuming the control to be given by Eq. (14).

On one hand the performance of the controller when a constant time-step is used may be very low, on the other hand, search for a minimizing time-step through online optimization procedure is cumbersome in the framework of actual control applications.

In order to increase the performance of the control without jeopardizing the computing time and resource of the controller, we propose an adaptive method to update the time-step.

Let call  $h_u$  the time-step computed assuming the current control to be  $u$ . Instead of searching for a minimizing time-step, we search for a time-step that may decrease the current value of the performance index using a gradient descent rule:

$$h_u(t+h) = h_u(t) - \alpha \left( \frac{\partial J}{\partial h} \right)_{h=h_u} \quad (16)$$

where  $h$  is the generic variable representing the time-step of the system and  $h_u$  is the actual time-step associated to the current control.

The step-size  $\alpha$  is defined by the designer and should be small enough to allow a reduction in the value of the performance index in the opposite direction of the gradient. In the analyzed model, it gives rise to a system based on the following equations:

$$\begin{aligned} x_1(t+h) &\approx x_1(t) + hf_1(x) + \frac{h^2}{2!} \frac{\partial f_1(x)}{\partial x} f(x) + \dots + \\ &+ \frac{h^{r_1-1}}{r_1!} \frac{\partial^{r_1-1} f_1(x)}{\partial x^{r_1-1}} f(x) \end{aligned} \quad (17)$$

$$\begin{aligned} x_2(t+h) &\approx x_2(t) + hf_2(x) + \frac{h^2}{2!} \frac{\partial f_2(x)}{\partial x} f(x) + \dots \\ &+ \frac{h^{r_2-1}}{r_2!} \frac{\partial^{r_2-1} f_2(x)}{\partial x^{r_2-1}} f(x) + \\ &+ \Lambda(h_u)W(x(t))u(t) \end{aligned} \quad (18)$$

where:

$$u(t) = -P^{-1} \left\{ \begin{array}{l} \frac{1}{2h_u^2} \left( \frac{\partial f_1(x)}{\partial x_1} B_2 \right)^T Q_1 \left( \begin{array}{l} e_1 + h_u \dot{e}_1 + \\ + \frac{h_u^2}{2!} \ddot{e}_1 \end{array} \right) + \\ + \frac{1}{h_u} B_2^T Q_2 (e_2 + h_u \dot{e}_2) \end{array} \right\} \quad (19)$$

$$P = \frac{1}{4} \left( \frac{\partial f_1(x)}{\partial x_2} B_2 \right)^T Q_1 \left( \frac{\partial f_1(x)}{\partial x_2} B_2 \right) + B_2^T Q_2 B_2 + h_u^{-4} R_2 \quad (20)$$

The effectiveness of this method will be shown in the following chapters.

### III. Development for Planar Navigation

#### III.1. Dynamic Model

The dynamic model used in this chapter is a 2D model suitable designing the controller. To be coherent with the development performed by Lu, the simulation describes a subsonic aircraft at constant speed  $V=150$  m/s.

The equations of motion are:

$$\dot{x} = V \cos \psi \quad (21)$$

$$\dot{y} = V \sin \psi \quad (22)$$

$$\dot{\psi} = \frac{g}{V} \tan \sigma \quad (23)$$

where  $x$  and  $y$  are position coordinates,  $\psi$  is the heading angle and  $\sigma$  is the bank angle. This bank angle is subject to the constraint:

$$|\sigma| \leq 80^\circ \quad (24)$$

#### III.2. Loiter Navigation

The first application of the controller is applied to a continuous system. The following application is similar to the one presented by Lu [7].

It was performed with the purpose of validating the implementation of the mathematical model reported above, and with a constant time-step and with a dynamic time-step.

In this section the dynamic time-step controller is named Controller I and the constant time-step controller is named Controller II. The reference trajectory is a circle of radius  $R$  defined by the equations:

$$\bar{x}(t) = R \cos \omega t \quad (25)$$

$$\bar{y}(t) = R \sin \omega t \quad (26)$$

$$\bar{\psi}(t) = \frac{\pi}{2} + \omega t \quad (27)$$

where  $R=1000$  m and  $\omega = \frac{V}{R} = 0.15$  rad/s.

The initial state of the aircraft is:

$$x(0) = \begin{Bmatrix} 0 \\ 0 \\ 0 \end{Bmatrix} \quad (28)$$

and the control defined as:

$$u = \tan \sigma \quad (29)$$

The weight matrices are set as:

$$Q_1 = \begin{bmatrix} 0.01 & 0 \\ 0 & 0.01 \end{bmatrix}, Q_2 = 0.01h^2, R_2 = 1 \quad (30)$$

Fig. 1 shows the tracking response of the system for  $h=0.5$ s. It demonstrates how the control dynamic time-step increases considerably performances of the controller in a dynamic tracking problem. Moreover, the following picture (Fig. 2) illustrates the tracking error of the system. Despite its large initial error, the trajectory reaches the reference easily. As previously it is possible to see the different response of the two controllers. The “dynamic” controller reaches the reference faster and without any oscillation. Instead, the error in case of constant time-step is characterized by a damping that yields a negligible value only after two oscillations.

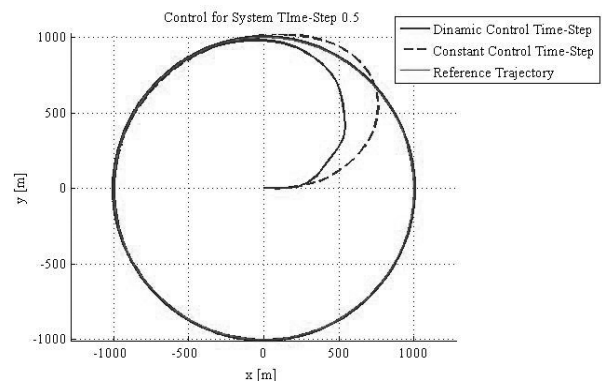


Fig. 1. 2D Loiter – Reference Trajectory Tracking

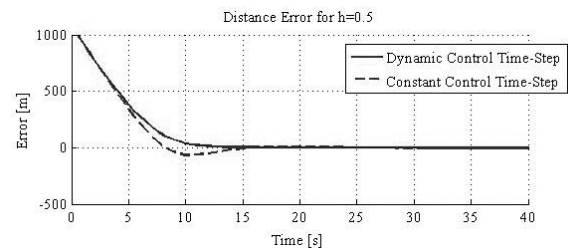


Fig. 2. 2D Loiter – Tracking Error

The control histories of the two controllers are compared in Fig. 3. Whereas the control variable  $u_{II}$  presents a smooth trend,  $u_I$  described two valleys that represent the correction necessary to ensure the desired status.

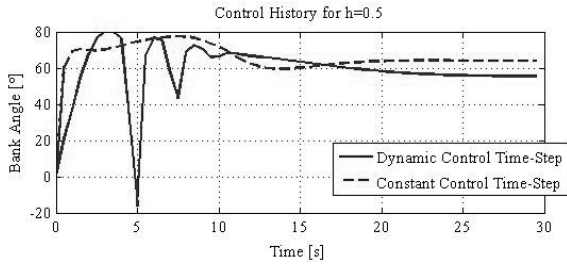


Fig. 3. 2D Loiter – Control History

Finally, the history of  $h_u$  is reported in Fig. 4. It smoothly approaches a value that will increase performances of the controller. Note that the step-size  $\alpha$  is defined as:

$$\alpha(i) = \frac{0.01}{i}, \quad \text{for } i = 1, \dots, n \quad (31)$$

$$\alpha = 0.0001, \quad \text{for } i > 100 \quad (32)$$

where  $n$  is the number of the steps required in the first 20 seconds, the value, which  $h_u$  will approach too, will not be the optimum control gain but it will simply give rise to an improvement of the controller performances.

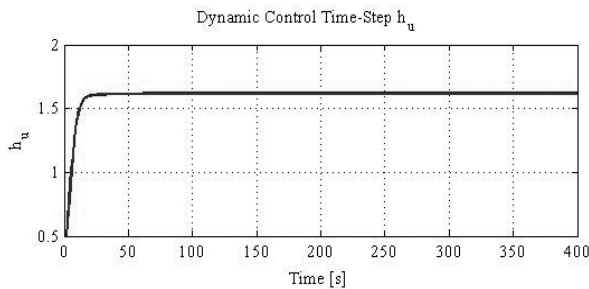


Fig. 4. 2D Loiter – Dynamic Control Gain Trend

### III.3. Planar Waypoint Navigation Using Model Predictive Control

The same model previously exposed has been implemented for a trajectory defined by waypoints. In this case the reference trajectory cannot be considered time-varying and, hence, all the considerations about the dynamic time-step will fall. Even if the implementation will remain the same as the previous one, the resulting control gain will be constant.

Waypoints are sets of coordinates that identify a point in physical space.

For the purpose of navigation, these coordinates usually include longitude and latitude, and sometimes altitude (particularly for air navigation).

Waypoints have only become widespread for navigation since the development of advanced navigational systems, such as the Global Positioning System (GPS) and certain other types of radio navigation. Waypoints located on the surface of the Earth are usually defined in two dimensions (e.g., longitude and latitude); those used in the Earth's atmosphere or in outer space are defined in at least three dimensions (four if time is one of the coordinate axis).

These waypoints are used to help define invisible routing paths for navigation. A waypoint can be a destination, a fix along a planned course used to make a journey, or simply a point of reference useful for navigation. In the following example the waypoint has been set as:

$$\begin{aligned} x_{ref} &= 500\text{m} \\ y_{ref} &= 1000\text{m} \end{aligned} \quad (33)$$

and the simulation will stop when

$$e \leq 50\text{m} \quad (34)$$

where  $e$  is the line-of-sight distance between the current position of the aircraft and the target waypoint, that is,  $e$  is computed as:

$$e = \sqrt{(x_{ref} - x)^2 + (y_{ref} - y)^2} \quad (35)$$

Once the waypoint is defined, the system will respond as illustrated in Fig. 5.

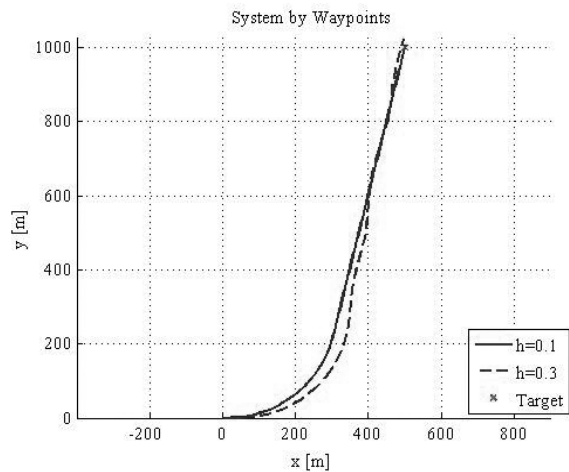


Fig. 5. Waypoint Tracking

It is possible to see how the choice of an appropriate time-step  $h$  is extremely important for the minimization of the final error and for a smooth response.

The control history is illustrated in Fig. 6. It is easy to see how the system is better controlled for a time-step  $h=0.1$ s. The following Fig. 7 shows an example of navigation by a three-waypoint set with excellent results.

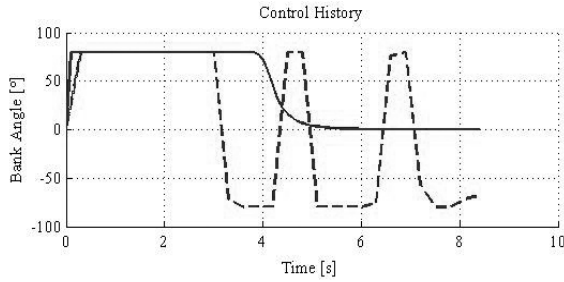


Fig. 6. Waypoint Tracking – Control History

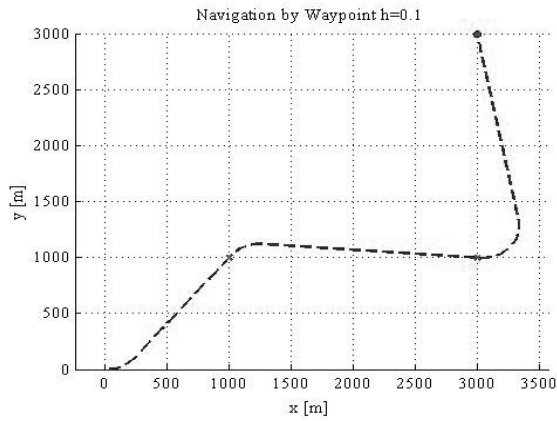


Fig. 7. Planar Navigation by Waypoint

The following Fig. 8 shows how the navigation is perfectly controlled.

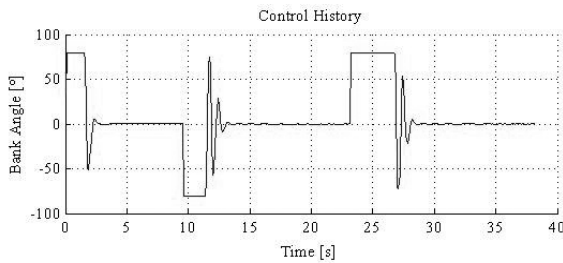


Fig. 8. Planar Navigation by Waypoint – Control History

### III.4. Waypoint Navigation with Variable Range

In order to lead the aircraft to the next waypoint, the model previously exposed has been provided with a variable waypoint range. To prevent overshoot when the aircraft has to switch from a waypoint to another, it is necessary that the switching operation occurs from a certain distance to the current waypoint.

The determination of that distance is based on the bearing of the current waypoint, as will be described hereafter. First of all the minimum radius of bank  $R_{min}$  is calculated in accordance with the constraint of  $|\sigma| \leq \bar{\sigma} = 80^\circ$  (Eq. (24)), that is:

$$R_{min} = \frac{V^2}{g \tan \bar{\sigma}} \quad (36)$$

Then, based on the waypoint set, we can determine the course from the current waypoint  $A$  to the next  $B$  from their coordinates as:

$$\psi_{AB} = \tan^{-1} \left( \frac{y_B - y_A}{x_B - x_A} \right) \quad (37)$$

Hence, the variation of the course (and therefore, of heading) will be

$$\Delta\psi = |\psi_{BC} - \psi_{AB}| \quad (38)$$

Finally the distance from which the switching to the next waypoint should occur is computed as:

$$R_{din} = R_{min} \tan(\Delta\psi) \quad (39)$$

Therefore, the aircraft will start to bank as soon as the distance to the current waypoint is less than  $R_{din}$ , that is, when:

$$\sqrt{(x_{wpt} - x_{aircraft})^2 + (y_{wpt} - y_{aircraft})^2} \leq R_{din} \quad (40)$$

where  $(x_{wpt}, y_{wpt})$  represents the coordinate position of the current waypoint, and  $(x_{aircraft}, y_{aircraft})$  that of the aircraft.

The navigation strategy that we have just described allows the aircraft to initiate turn at the right distance from the next waypoint, as shown in the Fig. 9.

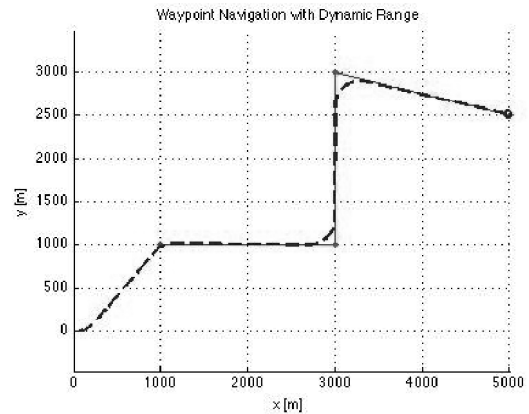


Fig. 9. Navigation by Waypoint with Variable Range

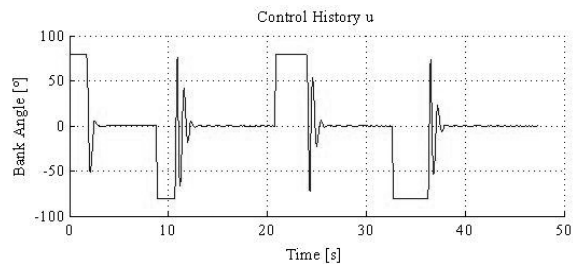


Fig. 10. Navigation by Waypoints with Variable Range – Control History

## IV. Development for Three-Dimensional Navigation

### IV.1. Dynamic Model

The dynamic model, used for the development of the 3D navigation, is a quasi-linearized model for small path angle  $\gamma$  :

$$\dot{x} = V \cos \psi \quad (41)$$

$$\dot{y} = V \sin \psi \quad (42)$$

$$\dot{z} = V \gamma \quad (43)$$

$$\dot{\psi} = \frac{g}{V} \tan \sigma \quad (44)$$

$$\dot{\gamma} = f(\delta) \quad (45)$$

being  $\delta$  the deflection of the vertical control surfaces,  $V$  the speed,  $\psi$  the heading,  $g$  the gravity acceleration,  $\sigma$  the bank angle. Let the controls be defined as:

$$u_1(t) = \tan \sigma \quad (46)$$

$$u_2(t) = f(\delta) \quad (47)$$

The model is subject to the following constraints:

- One constraint applied to the state, in particular on the flight path angle:

$$|\gamma| < 5^\circ \quad (48)$$

- Two other constraints applied to the controls:

$$|\sigma| \leq 80^\circ \text{ and } |\dot{\gamma}| \equiv |u_2| \leq 30^\circ/\text{s} \quad (49)$$

Therefore the model will be split into a state  $x_1$  composed of three elements and a state  $x_2$  composed of two elements, that is:

$$x_1 = \begin{Bmatrix} x \\ y \\ z \end{Bmatrix}, x_2 = \begin{Bmatrix} \psi \\ \gamma \end{Bmatrix} \quad (50)$$

### IV.2. Waypoint Navigation

First of all, the controller has been tested for a 3D navigation along fixed waypoints. Let:

$$Q_1 = \begin{bmatrix} 1 & 0 & 0 \\ 0 & 1 & 0 \\ 0 & 0 & \frac{1}{\varepsilon + e_z^2} \end{bmatrix}, Q_2 = \begin{bmatrix} h^2 & 0 \\ 0 & h^2 \end{bmatrix}, \quad (51)$$

$$R_2 = \begin{bmatrix} 1 & 0 \\ 0 & 1 \end{bmatrix}$$

where  $\varepsilon=10^{-6}$  is a parameter to prevent matrix  $Q_1$  from being singular,  $h$  is the time-step, and:

$$e_z = x_z - q_z$$

The error is defined as:

$$e = \sqrt{(x_{ref} - x)^2 + (y_{ref} - y)^2 + (z_{ref} - z)^2} \quad (52)$$

which is actually the distance between the aircraft and the next waypoint. The termination condition for the simulation is when:

$$e \leq 50\text{m} \quad (53)$$

Let consider the following waypoints:

$$q_1 = \begin{Bmatrix} 1000 \\ 0 \\ 0 \end{Bmatrix} \text{ and } q_2 = \begin{Bmatrix} 1000 \\ 1000 \\ 1000 \end{Bmatrix} \quad (54)$$

The aircraft reaches the second waypoint after a series of manoeuvres.

These are due to the saturation of the flight path angle since the system is considered for small angles. Below is reported the history of the two controls during the upward flight.

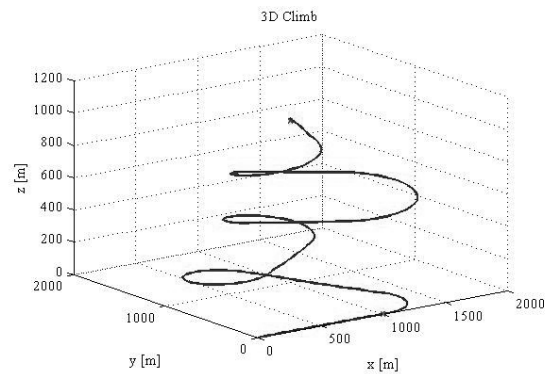


Fig. 11. 3D Climb – Isometric View

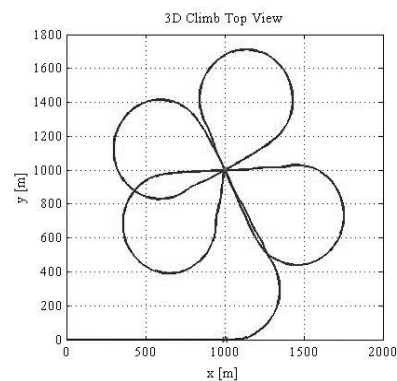


Fig. 12. 3D Climb – Top View

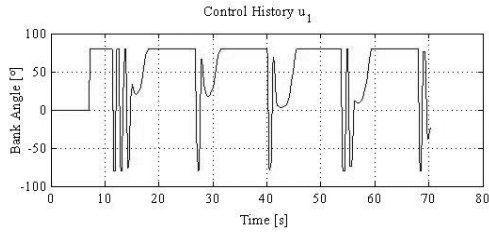


Fig. 13. 3D Climb – Control History  $u_1$

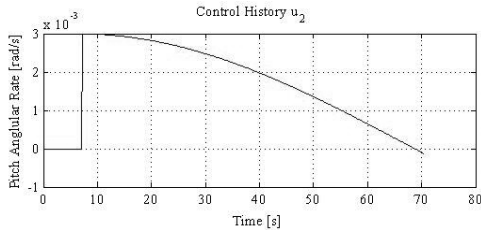


Fig. 14. 3D Climb – Control History  $u_2$

IV.3. Mission

Finally all the tests performed are joined in a simplified mission. Splitting the mission in three phases (climb – loiter – approach), the control is obtained by three different controllers specifically designed.

The simulation is run placing the three controllers in cascade. Each controller inputs the last state and control vectors of the previous one. Furthermore, the same data passing applies to the derivatives output in order to ensure the continuity of the derivatives.

Climb phase.

In this section the result for a 3D navigation along waypoints is reported. The original program has been implemented with the waypoint variable range as described in section III.4.

Fig. 15 shows how the aircraft perform the assigned navigation track moving perfectly along the path described by the waypoint set.

Fig. 17 shows the altitude of the aircraft during the flight. Oscillations are due to the transient phase and can be considered negligible. The peak of the oscillation is in fact less than 2% of the distance covered by the aircraft.

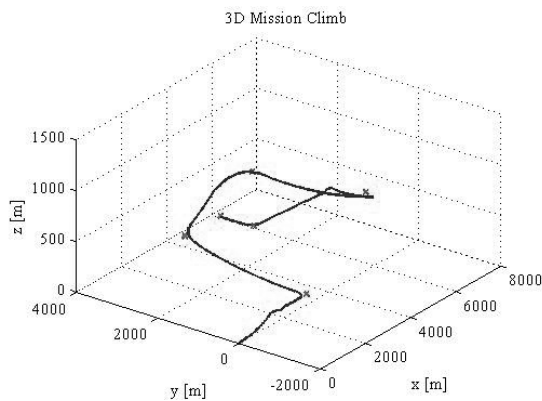


Fig. 15. Mission Climb – Isometric View

The behaviour of the control is illustrated in Figs. 18 and 19.

Loiter phase.

A loiter consists of a cruise flight for a certain amount of time over a specified area. The loiter phase occurs, for general aviation, generally at the end of the flight plan, normally when the plane is waiting for clearance to land.

However, some unmanned aircraft used for special purposes, like reconnaissance, monitoring or surveillance, may have a loiter phase in mid-flight.

STANAG 4586 [9] defines a set of loiter patterns along which a UAV should navigate in case of area surveillance and monitoring. These patterns are: circle, race-track, 8-shape (also called “Fig. 8”).

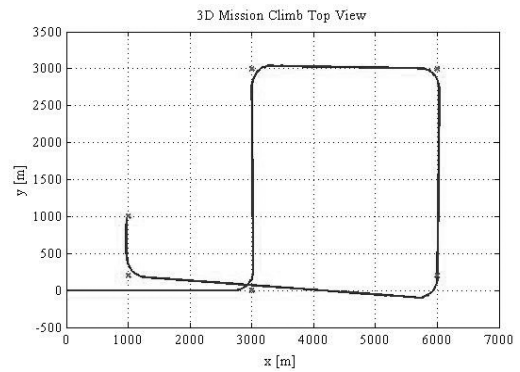


Fig. 16. Mission Climb – Top View

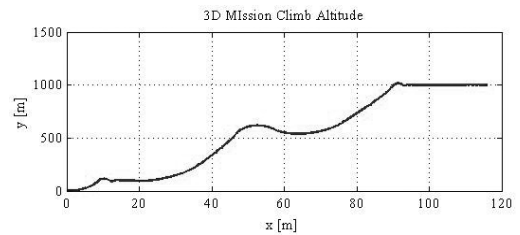


Fig. 17. Mission Climb – Altitude

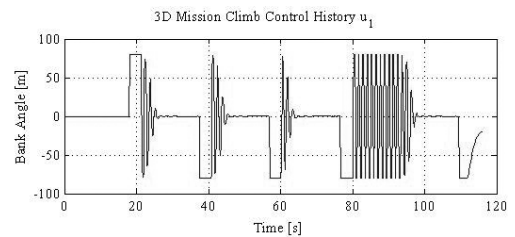


Fig. 18. Mission Climb – Control History  $u_1$

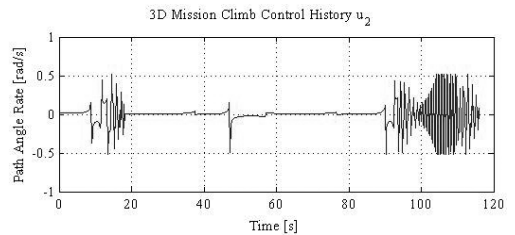


Fig. 19. Mission Climb – Control History  $u_2$

In general the flight altitude and the speed on a given loiter are kept constant during the mission.

The results of a circular loiter are described in this paragraph. That loiter is almost similar to the one reported in section III. The difference is that in the latter case the controller has to maintain the aircraft at a constant altitude. Therefore the trajectory will be described by the following continuous system:

$$\bar{x}(t) = R \cos \omega t \quad (55)$$

$$\bar{y}(t) = R \sin \omega t \quad (56)$$

$$\bar{z}(t) = \text{constant} \quad (57)$$

$$\bar{\psi}(t) = \frac{\pi}{2} + \omega t \quad (58)$$

where the variables have the same meaning as in section III.2,  $z$  being a constant altitude.

Let the controller parameters be:

$$Q_1 = \begin{bmatrix} 1 & 0 & 0 \\ 0 & 1 & 0 \\ 0 & 0 & \frac{1}{\varepsilon + e_z^2} \end{bmatrix}, \quad Q_2 = \begin{bmatrix} h^2 & 0 \\ 0 & h^2 \end{bmatrix}, \quad (59)$$

$$R_2 = \begin{bmatrix} 1 & 0 \\ 0 & 1 \end{bmatrix}$$

where the variables have the same meaning as in section IV.2 (Eq. (51)). Then, the trajectory of the aircraft is displayed in Figs. 20 and 21.

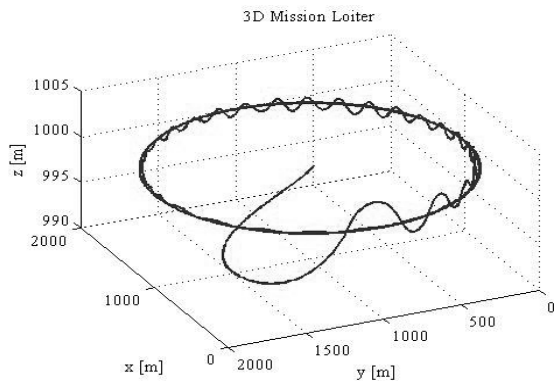


Fig. 20. Mission Loiter – Isometric View

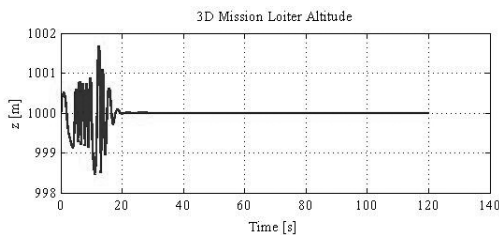


Fig. 21. Mission Loiter – Altitude

The control history of the transient is reported in Figs. 22 and 23.

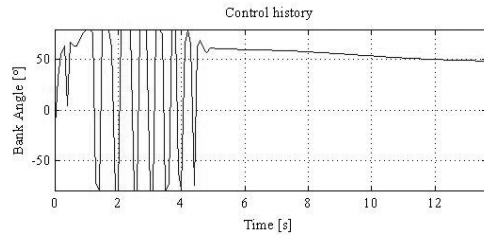


Fig. 22. Mission Loiter – Control History  $u_1$

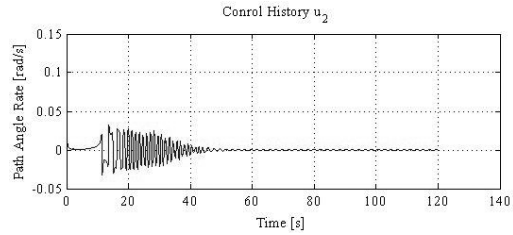


Fig. 23. Mission Loiter – Control History  $u_2$

*Approach phase.*

The approach phase is performed using the same principle as the one used for the climbing. The only difference is the waypoint set which is constant and set on:

$$q_1 = \begin{Bmatrix} 0 \\ 0 \\ 0 \end{Bmatrix} \quad (60)$$

## V. Discussion of the Results

As previously shown, the simulation results are clearly affected by the time-step parameter  $h$ . For this reason a preliminary study about  $h$  and  $Q$  influence is presented below.

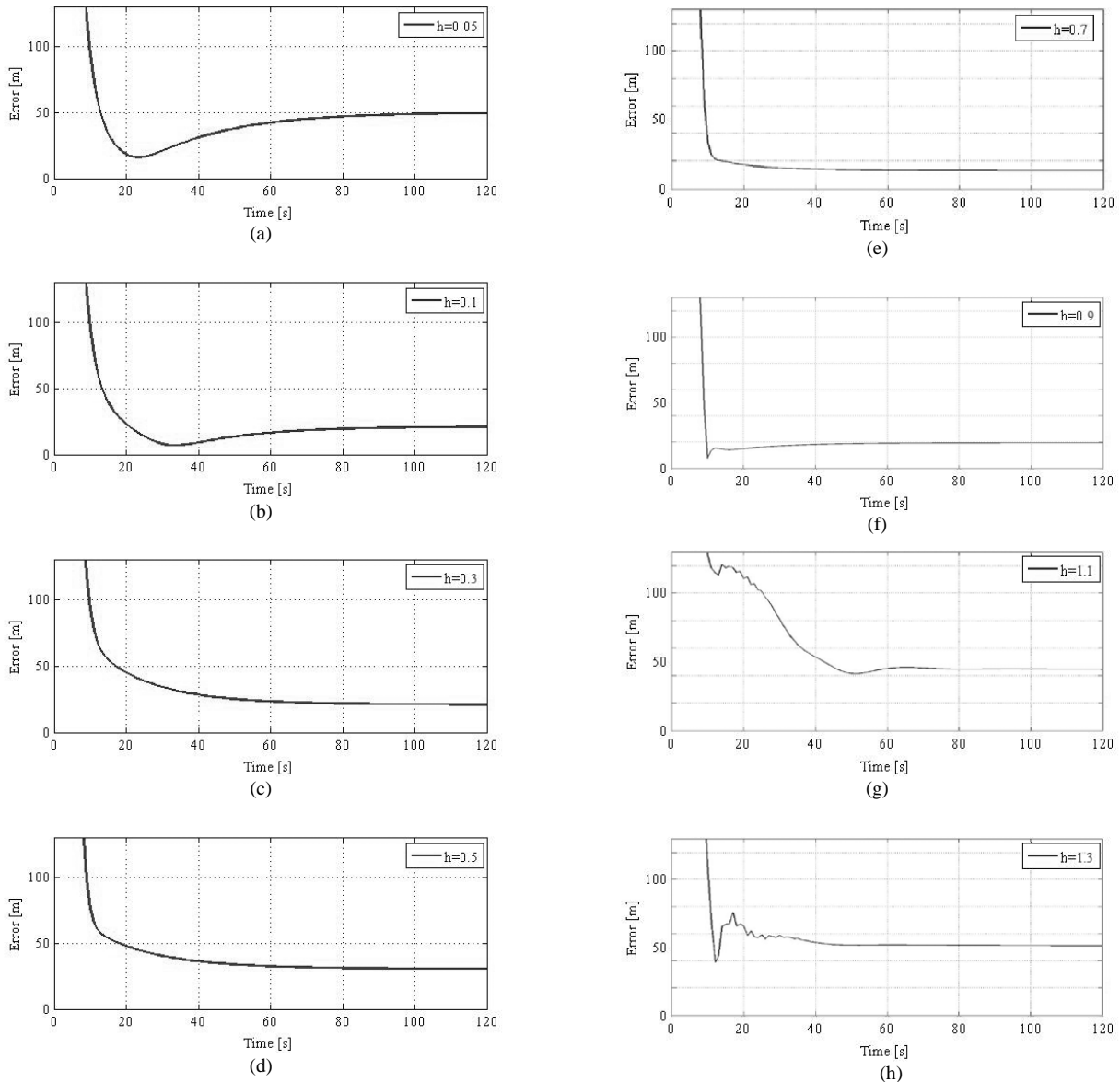
All the tests were performed changing only one parameter and keeping the other constant. The first parameter which is modified is the time-step  $h$ .

The way the time-step parameter affects the performance of the controller is depicted in a series of figures, all designated by Figs. 24, that show the loiter tracking error expressed as the deviation of the aircraft trajectory across-time with respect to the actual curve of the loiter.

Let the following parameters:

$$Q_1 = \begin{bmatrix} 0.01 & 0 \\ 0 & 0.01 \end{bmatrix}, \quad Q_2 = 0.01h^2, \quad R_2 = 1 \quad (61)$$

The value of  $h$  (time-step) that yields the minimum error after 2 minutes is  $h=0.1s$ . In spite of this, it doesn't reach the target trajectory as smoothly as when higher time-step values ( $h>0.1s$ ) are used. Furthermore, its transient state is longer than in most of the other cases.



Figs. 24. Error History for different system time-step  $h$

A better response is, instead, obtained setting the value  $h=0.7s$ . It reaches an error smaller than 20m in about 14s, afterwards it remains stable around the value of 13m.

From the value of  $h=0.9s$  it is possible to see how the response presents some oscillations during the transient phase. In particular, observing the response for  $h=1.1$  and  $h=1.3$ , despite bigger oscillations in the beginning, the steady-state errors are larger for higher values of  $h$  than for lower ones.

Matrix  $Q$  is another parameter that affects notably the response.

Let:

$$Q = c \begin{bmatrix} 1 & 0 & 0 \\ 0 & 1 & 0 \\ 0 & 0 & h^2 \end{bmatrix} \quad (62)$$

where  $c$  is a positive parameter.

The loiter tracking error dynamics are depicted in a series of figures for different values of parameter  $c$ , these are designated by Figs. 25.

First of all, a value suitable for the model had been found ( $c=0.01$ ).

Afterwards the parameter had been changed to analyze response variations.

It is easy to observe that the error significantly decreases when increasing the value of  $c$ .

With the highest value of  $c$ , it is possible to notice an oscillation during the first transient phase, similar to the one shown in Figs. 24.

Another interesting similarity is that, although the value of the test parameter ( $c=0.024$ ) is the highest, it causes a smaller oscillation during the transient phase but yields to a larger final error than in some other cases; for instance, when  $c = 0.022$ .

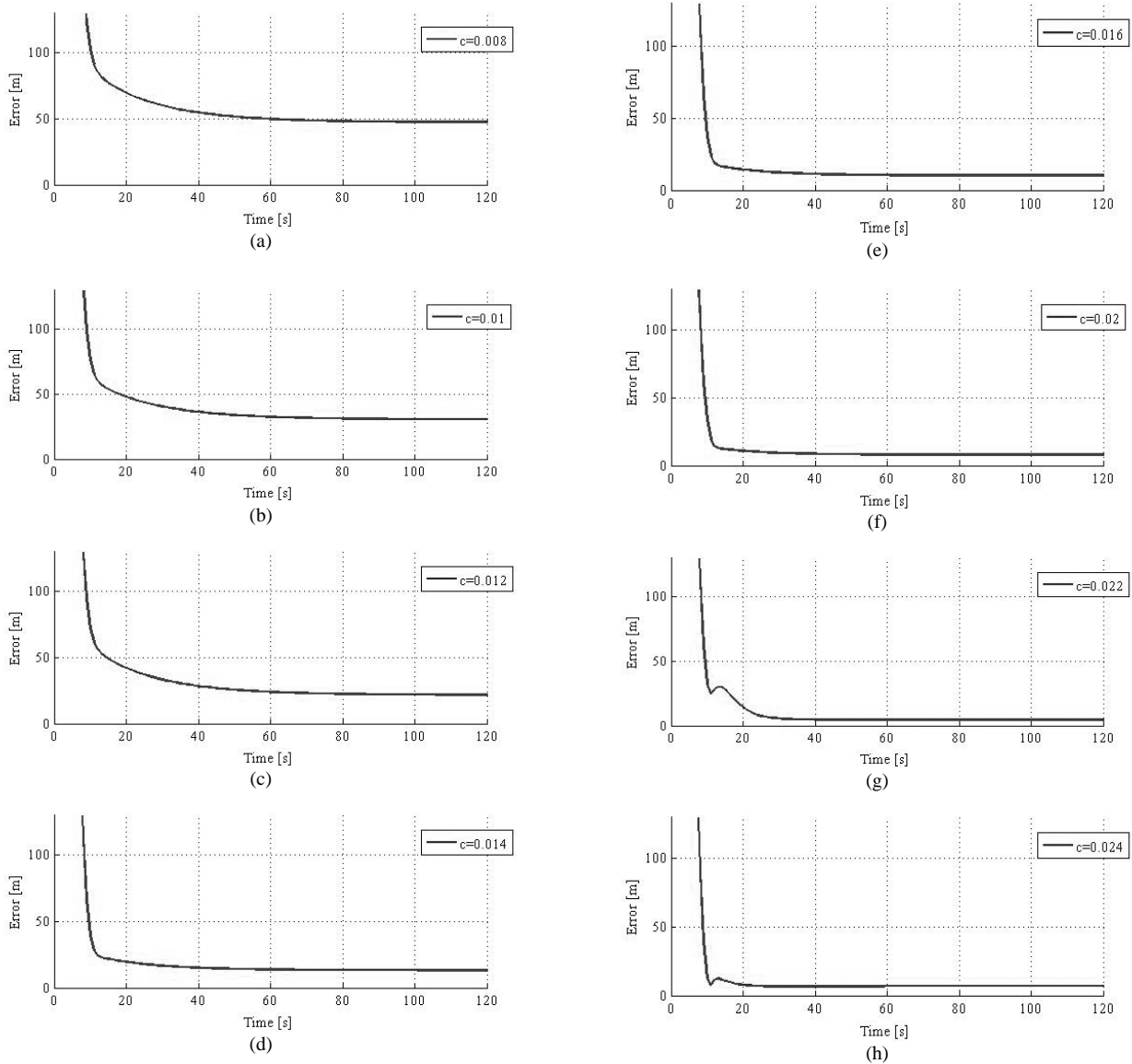


Fig. 25. Error History for different weighting Matrices Q

## VI. Conclusion

The presented method dealt with a nonlinear feedback control method based on Lie derivatives for UAV navigation guidance. This derives from a nonlinear predictive control concepts previously proposed by Lu and Khan [7], [8], but with an extension that we described that accounts for the adaptability of the time-step for the sake of improving the performance of the controller. Beyond the time-step adaptive update method, the paper described the various steps that were performed, in order to validate the navigation model along waypoints and on loiters.

The model was first tested for planar navigation on a circular loiter. The first sample dealt with a reference trajectory described by a continuous system. The second test concerned a planar navigation along waypoints and the third was a variable waypoint range model for a 3D navigation. The method was validated successfully on all

the scenarios related to the planar and three-dimensional navigation patterns including the circular loiter.

The design of the controller is not elementary. Controller parameters such as  $h$ ,  $Q$ ,  $R$  and  $\alpha$  used for the controller design actually affect the performance of the controller and a further study should be conducted as an extension to the present work.

We emphasize that this is the first work, to our knowledge, that uses Lie derivative based nonlinear control theory to solve systematically waypoint and loiter navigation problems.

The limitations of the presented method are that the adaptive time-steps were used for loiter navigation but could not be fully explored for waypoint navigation due to the discontinuity of the discrete reference trajectory.

Future work will aim at fully exploring the adaptive time-steps for waypoint navigation as well, so that adaptive control gains can be used not only for loiters but also for a waypoint sequence.

## Acknowledgements

This research was conducted in the Aeronautics and Astronautics Research Center (AeroG) at the University of Beira Interior in Covilhã, Portugal, and supported by the Portuguese Foundation for Sciences and Technology.

## References

- [1] B. L. Stevens, F. L. Lewis, *Aircraft Control and Simulation*, second ed. (John Wiley & Sons, Wiley, New York, 2003, pp. 403-484).
- [2] Isidori, *Nonlinear Control Systems*, third ed. (Springer-Verlag, New York, 1995).
- [3] R. Yanushevsky, *Modern Missile Guidance*, (CRC Press, Boca Raton, 2008)
- [4] W. Naeem, R. Sutton, S. M. Ahmad, R. S. Burns, A Review of Guidance Laws Applicable to Unmanned Underwater Vehicles, *The Journal of Navigation*, Vol. 56 (2003), 15-29.
- [5] T. S. No, B. M. Min, R. H. Stone, K. C. Wong, Control and Simulation of Arbitrary Flight Trajectory-tracking, *Control Engineering Practice*, Vol. 13 (2005), 601-612.
- [6] S. Bhat, P. Kumar, A Feedback Guidance Strategy for an Autonomous Mini-Air-Vehicle, *National Conference on Control and Dynamical Systems, IIT Bombay, India*, (2005).
- [7] P. Lu, Nonlinear Predictive Controllers for Continuous Systems, *Journal of Guidance, Control, and Dynamics Vol.17 No.3 (1994)*, 553-560.
- [8] M. A. Khan, P. Lu, New Technique for Nonlinear Predictive Control *Journal of Guidance, Control, and Dynamics Vol. 17 No 5 (1995)*, 1055-1060.
- [9] NATO, STANAG 4586 Ed. 2.5: Standard Interfaces for UAV Control Systems (UCS) for NATO UAV Interoperability (NATO Standardization Agency , Washington DC, 2007).

## Authors' information

<sup>1</sup>Politecnico di Milano, Facoltà di Ingegneria Aeronautica, 20100, Milano, Italia.

<sup>2</sup>Avionics & Control Laboratory, Department of Aerospace Sciences, University of Beira Interior, 6201-001 Covilhã, Portugal.  
Tel./Fax: (+351) 275 329 713 / Fax (+351) 275 329 768  
E-mails: [k1bousson@yahoo.com](mailto:k1bousson@yahoo.com)  
[bousson@ubi.pt](mailto:bousson@ubi.pt)



**G. Carloni** born in Jesi (AN), Italy on March 21<sup>st</sup>, 1982. He received his Laurea Triennale degree in Aerospace Engineering from the Politecnico di Milano, Milano, Italy, in 2005 and now is attending the Laurea Specialistica in the same university, with major in Avionics and Control Systems. Presently, He is collaborating with the Universidade da Beira Interior, Covilhã, Portugal, in the framework of the Erasmus program. He met in Portugal Prof. K. Bousson who supervised him for his first publication. Eng. Carloni already co-operated with Agusta Westland (Philadelphia, USA) and GlaxoSmithKline (Ware, UK) in previous working experiences.



**K. Bousson** received an MEng degree in aeronautical engineering from the Ecole Nationale de l'Aviation Civile (ENAC) in 1988, an MSc degree in computer science (with emphasis on artificial intelligence) from Paul Sabatier University in 1989, and a PhD degree in control & computer engineering from the Institut National des Sciences Appliquées (INSA) in 1993, all in Toulouse, France. He was a researcher at the LAAS Laboratory of the French National Council for Scientific Research (CNRS) in Toulouse, from 1993 to 1995, and has been a professor in the Department of Aerospace Sciences at the University of Beira Interior, Covilhã, Portugal, since 1995. His current research activities include analysis and control of nonlinear dynamical systems, trajectory optimization & guidance, and aerospace navigation systems. Dr. K. Bousson is a Member of the Armed Forces Communications and Electronics Association (AFCEA), and a Senior Member of the American Institute of Aeronautics and Astronautics (AIAA).

# A Dynamic Finite Element for Coupled Extensional-Torsional Vibration of Uniform Composite Thin-Walled Beams

S. M. Hashemi, A. Roach

**Abstract** – A Dynamic Finite Element (DFE) formulation for the free vibration analysis of extension-torsion coupled uniform composite thin-walled beams is presented. Employing the exact solutions of the differential equations governing the uncoupled vibrations of a uniform beam element, the analytical expressions for extensional and torsional dynamic trigonometric shape functions are derived. By exploiting the principle of virtual work and the frequency-dependent shape functions, the element dynamic stiffness matrix is developed. The application of the theory is demonstrated by a Circumferentially Uniform Stiffness (CUS) composite circular tube for which the influence of ply fibre-angle on the natural frequencies is studied. A variety of CUS configurations are studied and the correctness of the theory and the superiority of the proposed DFE over the conventional FEM methods are confirmed by numerical checks and the published results. **Copyright © 2016 Praise Worthy Prize S.r.l. - All rights reserved.**

**Keywords:** Composite Beam, Extension-Torsion Couplings, Dynamic Finite Element (DFE), Dynamic Stiffness Matrix (DSM), Finite Element Method (FEM), Materially Coupled Vibrations

## Nomenclature

$e$	Element index	$[\bar{M}]$	Global mass matrix
$E$	Young's modulus of elasticity	$sign[ ]$	Sign count, or Number of negative elements on main diagonal of a matrix
$F$	Axial force on member	$\{U\}$	Element displacement vector
$I$	Mass moment of inertia per unit length	$\{\bar{U}\}$	Global displacement vector
$J$	Total number of natural frequencies below a trial value	$W$	Total Virtual Work (VW)
$J_0$	Total number of system's CL/CL frequencies below a trial value	$W_{INT}$	Internal Virtual Work (VW)
$J_m$	Number of element CL/CL frequencies below a trial value	$W_{EXT}$	External Virtual Work (VW)
$L$	Member length	$W^e$	Element 'e' Virtual Work (Extension)
$m$	Mass per unit length	$\alpha$	DFE shape function variable (Virtual parameter (e.g., displacement))
$N$	Shape (Interpolation) functions	$\delta$	Poisson's ratio
$NoE$	Number of Elements	$\nu$	Circular frequency
$T$	Torque on member	$\omega$	Rotational displacement of member
$u$	Axial displacement of member	$\theta$	Amplitude of rotational displacement
$U$	Amplitude of axial displacement	$\Theta$	DFE shape function variable (Torsion)
$[F]$	Element force matrix	$\tau$	Non-dimensionalized length
$[K]$	Element stiffness matrix	$\xi = x/l$	
$[\bar{K}]$	Global Stiffness matrix		
$[\bar{K}(w)^\Delta]$	Upper triangularized stiffness matrix		
$[k(\omega)]_{Uncoupled}^e$	Frequency dependent, element 'e' dynamic stiffness matrix		
$[k(\omega)]_{Uncoupled}^e$	Uncoupled matrix terms in $[k(\omega)]^e$		
$[k(\omega)]_{Coupling}^e$	Coupling matrix terms in $[k(\omega)]^e$		
$[M]$	Element mass matrix		

## I. Introduction

Certain structural members exhibit coupled extension-torsion behaviour when subjected to static or dynamic loads. In other words, under the action of an applied torsional moment, the element undergoes simultaneous angular and axial displacements. Similarly, an axial load causes both extensional and rotational displacements in the element. Such members include closed section thin-walled laminated composite beams and tubes formed by wrapping a laminate and joining its longitudinal edges

together to form a cross-section which, except from the stacking sequence of plies, is doubly symmetric; e.g., square, rectangular, circular or elliptical tubes (Fig. 1).

For obvious advantages such as the high strength to weight ratio and high stiffness to weight ratio, fibre reinforced laminated composite thin-walled beam structures are likely to play a decisive role in the design of the actual and specially future generations of aeronautical and aerospace structures. The structural and dynamic behaviour of such structural members are therefore of great significance and have attracted special attention. Interest shown by many investigators concentrates on different aspects related to design, analysis and optimisation of such structural elements, with especial regards to buckling, free and forced vibration characteristics, and aeroelastic response of composite beams and tubes. Certain researchers are concerned by the theoretical development and/or experimental validation of the relevant governing equations of motion, whereas others rely on exact or approximate numerical methods to solve these equations.

Nixon investigated the extension-twist coupling of composite circular tubes with application to tilt rotor blade design [1].

Song and Liberscu [2] studied the free vibration and aeroelastic divergence of aircraft wings modelled as Circumferentially Uniform Stiffness (CUS) composite thin-walled box beams, for which the effective reduced material stiffness terms are constant around the cross section. The effects of ply-angles on the coupled extension-torsion coupled modes and divergence speed were investigated. Static structural response of two-cell blades, with extension-torsion couplings [3] and the torsional actuation of a rotor blade trailing-edge flap, in conjunction with a composite tube have also been addressed [4].

Smith [5] investigated the vibration and flutter of elastically tailored composite blades and the influence of extension-torsion elastic and ply-induced composite couplings on the blade stability. Banerjee and his colleagues proposed an exact Dynamic Stiffness Matrix (DSM) method to investigate the free vibration characteristics of extension-torsion coupled composite beams [6] and structural members [7]. Bhaskar and Liberscu [8] studied the flexural buckling of single-cell extension-twist coupled beams under axial compression. Cesnik *et al.* [9] presented an aeroelastic stability analysis for high-aspect ratio composite wings, where the importance of material couplings, static aeroelastic tailoring, and the variation of static instability (i.e., divergence speed) with ply angle for CUS configuration wing box were discussed [9]. Kosmatka and Lake [10] examined the structural and free vibration behaviour of initially twisted composite spars for tilt-rotor applications.

Analytical and a detailed FEM models were used to investigate the effect of geometry, material orientation, and material-based extension-twist couplings on the spar behaviour.

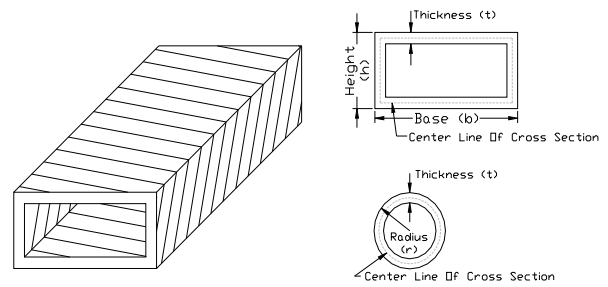


Fig. 1. Circular tube and box-beam cross-sections

Some other examples of extension-torsion structural elements, each governed by different equations of motion, have also been reported in the literature [11]-[15]. This work is partly motivated by earlier works and presents the derivation of a Dynamic Finite Element (DFE) for the free vibration analysis of a uniform composite structural member exhibiting coupled torsional-extensional behaviour.

Starting with basic governing differential equations, the Dynamic Trigonometric Shape Functions (DTSFs), also satisfying the governing differential equations of motion in free uncoupled vibration of the member, are first developed. These shape functions, in conjunction with the FEM formulation, are then used to find the frequency-dependent element stiffness matrices.

Assembly of the element matrices and application of boundary conditions generates the global dynamic stiffness matrix, which in turn leads to the nonlinear eigenvalue problem of the system. By solving the resulting eigenproblem, one can then evaluate the natural frequencies and modes of vibration of composite tubes and beam-structures. Based on the proposed DTSFs, the weighted residual method and the principle of virtual work (PVW), it will be possible to extend the DFE method to more complex cases including variable structural, material, and mechanical parameters. This fact distinguishes DFE formulation from the exact DSM method. In what follows, the application of the DFE approach with particular reference to an established root counting algorithm is discussed [16].

Numerical DFE results for coupled natural frequencies and modes of vibration of a set of composite circular tubes are evaluated and compared with existing exact DSM results and those obtained from the conventional FEM.

## II. Mathematical Model

The derivation of the equations of motion for the coupled extension-torsion vibrations of composite beams, formed by continuous winding of fibres with symmetric but unbalanced lay-ups, are studied by different authors (see, e.g., [6]) and various approaches for calculating the free vibration natural frequencies and mode shapes have been proposed.

Such a structural member has been characterized in the literature [6], [17]-[19] by its equivalent extensional

rigidity,  $\kappa_1$ , coupled extension-twist stiffness,  $\kappa_{12}$ , and the torsional rigidity,  $\kappa_2$  (see Appendix I for details).

The differential equations of motion governing the free, coupled torsional-extensional vibration of a composite tube or box-beam can then be written as [6], [7], [20]:

$$\kappa_1 U_{xx} + \kappa_{12} \theta_{xx} + m\omega^2 U = 0 \quad (1)$$

$$\kappa_{12} U_{xx} + \kappa_2 \theta_{xx} + I_\alpha \omega^2 \theta = 0 \quad (2)$$

obtained based on the usual simple harmonic motion assumption:

$$u(x,t) = U(x) \sin \omega t \quad (3)$$

$$\theta(x,t) = \Theta(x) \sin \omega t \quad (4)$$

with appropriate boundary conditions imposed at  $x=0, L$ .

For example:

- Clamped at  $x=0$ ;  $U(x=0) = 0$ ,  $\Theta(x=0) = 0$ ,
- Free at  $x=L$ ; axial force,  $F(x=L) = \kappa_1 U' + \kappa_{12} \Theta' = 0$ , and torque,  $T(x=L) = \kappa_{12} U' + \kappa_2 \Theta' = 0$ , etc.  $U(x)$  and  $\Theta(x)$  represent the amplitudes of axial and torsional displacements, respectively.

Application of Galerkin-type integral weighted residual formulation on Eqs. (1) and (2), leads to:

$$W_U = \int_0^L \delta U (m\omega^2 U + \kappa_1 U_{xx} + \kappa_{12} \Theta_{xx}) dx = 0 \quad (5)$$

$$W_\Theta = \int_0^L \delta \Theta (I\omega^2 \Theta + \kappa_{12} U_{xx} + \kappa_2 \Theta_{xx}) dx = 0 \quad (6)$$

where  $\delta U$ ,  $\delta \theta$ , and  $U$ ,  $\theta$ , are the axial and torsional virtual displacements and field variables, respectively, expressed within the same approximation space.

Integrating by parts leads to alternative representation of Eqs. (5) and (6) as:

$$W_U = - \int_0^L (\delta U_x (\kappa_1 U_x + \kappa_{12} \Theta_x) + \delta U m \omega^2 U) dx + [\delta U (\kappa_1 U_x + \kappa_{12} \Theta_x)]_0^L = 0 \quad (7)$$

$$W_\Theta = - \int_0^L (\delta \Theta_x (\kappa_{12} U_x + \kappa_2 \Theta_x) + \delta \Theta I \omega^2 \Theta) dx + [\delta \Theta (\kappa_{12} U_x + \kappa_2 \Theta_x)]_0^L = 0 \quad (8)$$

which also satisfy the Principle of Virtual Work (PVW):

$$W = W_{INT} + W_{EXT} = 0 \quad (9)$$

Considering free vibrations, there is no external force applied to the system, which leads to  $W_{EXT} = 0$ , and as a result  $W = W_{INT} = 0$ . Enforcing the displacement and force boundary conditions makes the boundary terms in (7) and (8) vanish [17], [21]-[24].

Discretization of the domain into a certain number of 2-node, four degree-of-freedom beam elements, ( $NoE$ ), then leads to (Fig. 2):

$$W = W_{INT} = \sum_{e=1}^{NoE} (W_U^e + W_\Theta^e) = 0 \quad (10)$$

where:

$$W^e = W_U^e + W_\Theta^e$$

and:

$$W_U^e = \int_0^1 \left( \delta U m \omega^2 U - \frac{\delta U_\xi}{l^2} (\kappa_1 U_\xi + \kappa_{12} \Theta_\xi) \right) l d\xi \quad (11)$$

$$W_\Theta^e = \int_0^1 \left( \delta \Theta I \omega^2 \Theta - \frac{\delta \Theta_\xi}{l^2} (\kappa_{12} U_\xi + \kappa_2 \Theta_\xi) \right) l d\xi \quad (12)$$

where  $dx = l d\xi$ ,  $d(\Gamma)/dx = d(\Gamma)/(l) d\xi$ , and  $l$  is the element length. Each element 'e' is defined by nodes  $j$  and  $j+1$  with corresponding coordinates ( $l = x_{j+1} - x_j$ ).

The admissibility requirement for finite element approximation is controlled by (7) and (8).

The approximation space must satisfy  $C^0$ -type continuity, assuring continuity of  $U$  and  $\Theta$  at each node. Expressions (11) and (12) simply present discretized form of (7) and (8), evaluated at the element level.

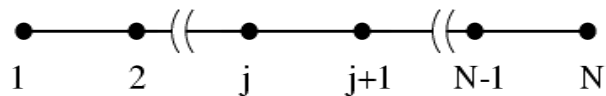


Fig. 2. Domain discretized by 2-node elements

### II.1. Classical Finite Elements Method

The classical FEM model is found by using a linear polynomial approximation such as:

$$\Theta(x) = N_1(x) \Theta_1 + N_2(x) \Theta_2 \quad (13)$$

where  $\Theta_1$  and  $\Theta_2$  are nodal values of torsional displacements at nodes  $j$  and  $j+1$ , respectively. For axial displacement,  $U(x)$ , and virtual variables  $\delta U$  and  $\delta \Theta$ , one uses similar (linear) approximations. Assembly of Eqs (11) and (12) and application of B.C. lead to:

$$W = W_{INT} = \sum_{e=1}^{NoE} W^e = \sum_{e=1}^{NoE} ([K] - \omega^2 [M]) \{U\} = 0 \quad (14)$$

or:

$$([\bar{K}] - \omega^2 [\bar{M}]) \{\bar{U}\} = 0 \quad (15)$$

which is a linear eigenvalue problem (in  $\omega^2$ ), and a function of constant mass and stiffness matrices.

Several powerful algorithms exist for solving a linear eigenvalue problem (15) resulting from discrete or lumped mass models [22]. In this study, both “eig” function available in Matlab® and the well-known Wittrick-Williams (W-W) algorithm were used to solve the eigenproblem (15).

### II.2. The Dynamic Finite Element (DFE) Formulation

When the elemental parameters,  $\kappa_1$ ,  $\kappa_{12}$ ,  $\kappa_2$ ,  $m(x)$ , and  $I$ , are all constant, it is then possible to obtain a general solution for  $u$  and  $\theta$  that leads to an exact Dynamic Stiffness Matrix (DSM) [6], [7].

For harmonic oscillation, the two coupled governing Eqs. (1) and (2) are combined into one 4<sup>th</sup> order ordinary differential equation, which applies to both axial and torsional displacements. A closed form analytical solution is then sought in its most general form [6] and by applying the boundary conditions, the system’s DSM is developed. However, when the beam geometric and mechanical properties are not constant, it becomes cumbersome or even impossible to obtain the exact model. The approximation space, in this case, depends on the nature of the space variation of these parameters.

In this study, we propose a hybrid numerical method in which the classical FEM and DSM are combined to obtain a better FEM model. The approximation space is defined by the frequency-dependent trigonometric functions, where the solutions of the uncoupled governing differential equations of motion are utilized as dynamic basis functions of approximation space.

The resulting shape functions are then used to obtain the corresponding element stiffness matrix. In what follows, the dynamic finite element (DFE) is developed and demonstrated for the case of a uniform coupled composite beam, where the coefficients  $k_1$ ,  $k_{12}$ , and  $k_2$  are constant over the element.

The proposed DFE can also be directly applied to stepped configurations. The advantage of the proposed methodology over DSM is that the DFE can be extended to more complex cases such as coupled beams with nonuniform geometry and variable properties, exhibiting linear angle of twist. To this end, the interesting features of the DFE methodology presented in the earlier works of the first author, can be exploited (see, e.g., [21], [23], [24]).

To obtain the DFE formulation, a second integration by parts is applied to the element Eqs. (11) and (12) leading to the following equivalent form:

$$W_U^e = \int_0^1 U \left( \underbrace{\frac{\kappa_1 \delta U_{\xi\xi}}{l^2} + m\omega^2 \delta U}_{*} \right) l d\xi + \left[ \frac{\kappa_1}{l} \delta U_{\xi} U \right]_0^1 - \int_0^1 \frac{\kappa_{12}}{l} \delta U_{\xi} \theta_{\xi} d\xi \quad (16)$$

$$W_{\Theta}^e = \int_0^1 \theta \left( \underbrace{\frac{\kappa_2 \delta \theta_{\xi\xi}}{l^2} + I\omega^2 \delta \theta}_{**} \right) l d\xi + \left[ \frac{\kappa_2}{l} \delta \theta_{\xi} \theta \right]_0^1 - \int_0^1 \frac{\kappa_{12}}{l} \delta \theta_{\xi} U_{\xi} d\xi \quad (17)$$

The interpolation functions are then chosen such that they make vanish the first integral terms in (16) and (17); (\*), (\*\*) $\rightarrow 0$ . Then, the non-nodal approximations for  $U$  and  $\Theta$  are written as:

$$U(\xi) = C_1 \cos(\alpha\xi) + C_2 \sin(\alpha\xi) = \langle \cos(\alpha\xi) \quad \sin(\alpha\xi) / \alpha \rangle \begin{Bmatrix} A_1 \\ A_2 \end{Bmatrix} \quad (18)$$

$$\theta(\xi) = D_1 \cos(\tau\xi) + D_2 \sin(\tau\xi) = \langle \cos(\tau\xi) \quad \sin(\tau\xi) / \alpha \rangle \begin{Bmatrix} A_3 \\ A_4 \end{Bmatrix} \quad (19)$$

where  $\alpha = \omega l \sqrt{m / \kappa_1}$ ,  $\tau = \omega l \sqrt{I / \kappa_2}$ , and the coefficients  $C_{1,2,3,4}$  and  $A_{1,2,3,4}$  are constant parameters of non-nodal approximations with no physical meaning. It is worth noting that when  $\omega \rightarrow 0$ , then both  $\alpha$  and  $\tau \rightarrow 0$ .

Consequently the trigonometric expansion terms in expressions (18) and (19), representing the basis functions of approximation space, change to  $\langle 1 \xi \rangle$ , which are the classical linear polynomial ones used in the standard FEM.

The field variables and virtual displacements are both defined within the same approximation space. The nodal approximations based on the dynamic frequency dependent shape (interpolation) functions can then be written as:

$$U(\xi) = \langle N_{1a} \quad N_{2a} \rangle \begin{Bmatrix} U_1 \\ U_2 \end{Bmatrix} \quad (20)$$

$$\theta(\xi) = \langle N_{1t} \quad N_{2t} \rangle \begin{Bmatrix} \theta_1 \\ \theta_2 \end{Bmatrix}$$

where  $U_1$ ,  $U_2$ ,  $\Theta_1$  and  $\Theta_2$  represent the element nodal displacements.

The dynamic shape functions of approximation for extensional and torsional displacements are:

$$N_1(\omega)_a = \frac{\sin(\alpha(1-\xi))}{\sin(\alpha)}, \quad N_2(\omega)_a = \frac{\sin(\alpha\xi)}{\sin(\alpha)} \quad (21)$$

and:

$$N_1(\omega)_t = \frac{\sin(\tau(1-\xi))}{\sin(\tau)}, \quad N_2(\omega)_t = \frac{\sin(\tau\xi)}{\sin(\tau)} \quad (22)$$

Expressing the filed and virtual displacements using the dynamic shape functions (21) and (22) and putting them back in (16) and (17) will then make the first integral terms vanish and consequently one can write:

$$W_U^e = \langle \delta U_1 \quad \delta U_2 \rangle \left( \frac{\kappa_1}{l} \begin{bmatrix} -N'_{1\alpha \xi=0} & N'_{1\alpha \xi=1} \\ -N'_{2\alpha \xi=0} & N'_{2\alpha \xi=1} \end{bmatrix} \begin{bmatrix} u_1 \\ u_2 \end{bmatrix} \right) + \frac{\kappa_{12}}{l} \int_0^1 \begin{bmatrix} N'_{1\alpha} N'_{1\tau} & N'_{1\alpha} N'_{2\tau} \\ N'_{2\alpha} N'_{1\tau} & N'_{2\alpha} N'_{2\tau} \end{bmatrix} d\xi \begin{bmatrix} \theta_1 \\ \theta_2 \end{bmatrix} \quad (23)$$

and:

$$W_\Theta^e = \langle \delta \theta_1 \quad \delta \theta_2 \rangle \left( \frac{\kappa_2}{l} \begin{bmatrix} -N'_{1\tau \xi=0} & N'_{1\tau \xi=1} \\ -N'_{2\tau \xi=0} & N'_{2\tau \xi=1} \end{bmatrix} \begin{bmatrix} \theta_1 \\ \theta_2 \end{bmatrix} \right) + \frac{\kappa_{12}}{l} \int_0^1 \begin{bmatrix} N'_{1\tau} N'_{1\alpha} & N'_{1\tau} N'_{2\alpha} \\ N'_{2\tau} N'_{1\alpha} & N'_{2\tau} N'_{2\alpha} \end{bmatrix} d\xi \begin{bmatrix} u_1 \\ u_2 \end{bmatrix} \quad (24)$$

The last two expressions are then combined to obtain a single dynamic stiffness matrix governing the coupled extensional-torsional vibrations of the composite beam:

$$W^e = \langle \delta u_n \rangle_{1 \times 4} [k(\omega)]_{4 \times 4}^e \{u_n\}_{4 \times 1} \quad (25)$$

where:

$$[k(\omega)]^e = [k(\omega)]_{Uncoupled}^e + [k(\omega)]_{Coupling}^e \quad (26)$$

$[k(\omega)]_{Uncoupled}^e$  is the frequency dependent DFE stiffness matrix for element 'e'.  $[k(\omega)]_{Uncoupled}^e$  and  $[k(\omega)]_{Coupling}^e$  represent the first (uncoupled) and the second (coupling) matrix terms in expressions (23) and (24), respectively. All the components in the coupled matrix are integrated symbolically to ensure the final DFE matrix is purely algebraic. This practice decreases the computational time extensively. Taking the boundary conditions into account, the total  $W$  is then the sum of element  $W^e$  over the number of elements.

It can be readily verified from expressions (23)-(26) that  $[k(\omega)]_{Coupling}^e$  reduces to zero when  $\kappa_{12}=0$ .  $\kappa_{12}=0$

can be substituted in the derived expressions without causing any overflow or underflow. The element matrix (26) then reduces to the exact DSM for uncoupled axial and torsional vibrations of a uniform rod or bar element.

Furthermore, when  $\omega \rightarrow 0$ , the shape functions (20)-(22) reduce to the linear polynomial shape functions,  $\langle 1-\xi \quad \xi \rangle$ , commonly used in conventional FEM. The element DSM (26) then changes to the constant stiffness matrix of a bar element, undergoing uncoupled extension and torsion (see, e.g., [22]). The DFE developed here, covers the materially coupled extensional-torsional vibrations of a uniform CUS composite beam element.

The geometric and material parameters were all assumed to be constant per element. Based on the proposed formulation, one can also model the vibration behaviour of piecewise uniform, or stepped, circumferentially uniform stiffness composite beams.

However, the theory is not limited to those geometries and the effects of variable geometric parameters and mechanical properties can be introduced in a *refined* formulation by using similar techniques as presented in [21], [23]-[25].

### II.3. Application of the Theory and Calculation of Natural Frequencies

The standard assembly process similar to (14) leads to the expression of total virtual work as:

$$W = \langle \delta \bar{U} \rangle [K(\omega)] \{ \bar{U} \} = 0 \quad (27)$$

Expression (27) also represents nonlinear eigenvalue problem of the system, where  $[K(\omega)]$  is the global dynamic stiffness matrix. The eigenvalue,  $\omega$ , and corresponding eigenvector,  $\{ \bar{U} \}$ , are then to be found.

They must make  $W$  vanish for any arbitrary virtual displacement,  $\langle \delta \bar{U} \rangle$ , while satisfying the boundary conditions. This leads to:

$$[\bar{K}(\omega)] [\bar{U}] = [0] \quad (28)$$

The nonlinear eigenproblem (28) involves frequency-dependent dynamic stiffness matrices arising from the DFE or DSM formulations. To find the natural frequencies of a system governed by (28), one can use the W-W root-finding technique [16] (see Appendix II for more details).

## III. Numerical Tests

On the basis of the analytical and numerical procedures presented in the previous sections, Matlab<sup>®</sup> codes have been written and representative examples

have been studied to demonstrate the efficiency, wherever possible the accuracy and the range of applications of the developed DFE method. The DSM and classical FEM methods were also programmed.

The coupling integral terms in the DFE element stiffness matrix (26) were initially calculated using a 12-point Gauss Quadrature numerical integration [22]-[25].

The program was then optimised by symbolically integrating each element of  $[K(\omega)]^{e}_{Coupling}$  to evaluate the natural frequencies and modes of materially coupled thin-walled CUS composite tubes (Fig. 3).

The effective reduced material stiffness terms  $A(s)$ ,  $B(s)$  and  $C(s)$ , in this case, are constant around the cross section (refer to [17], [25], [26]) and the stiffness parameters of interest are:  $\tau_1=C_{11}=Al_c$ ,  $\tau_{12}=C_{12}=BA_e$ ,  $\tau_2=C_{22}=CA_e^2/l_c$ , where  $l_c=2\pi(r-t/2)$  is the length of the centreline of the cross section,  $A_e=\pi(r-t/2)^2$  is the area enclosed by the contour,  $m=2\pi\rho r t$  and  $I=2\pi r^3$  are the mass per unit length and the mass moment of inertia per unit length, respectively.

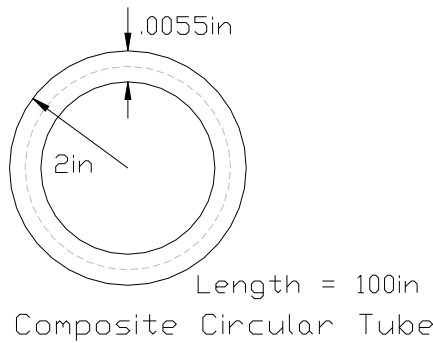


Fig. 3. Beam cross-sectional dimensions; uniform circular tube

In this section, an illustrative example of extension-torsion coupled cantilevered composite beam presented by Atiligan *et al.* [27], is investigated. The comparison is made between the DFE natural frequencies, the exact DSM results, the conventional FEM and the data available in the literature.

The CUS configuration circular tube, is made of a single laminate of T300/5208 Graphite/epoxy and has a length  $L=254$  cm and a total thickness of 0.1397 cm, with material properties as:  $E_1=146.858$  GPa,  $E_2=11.0316$  GPa,  $G_{12}=6.41212$  GPa,  $\nu_{12}=0.38$ , and  $\rho=1604.103$  kg/m<sup>3</sup>.  $E_1$  and  $E_2$  are the modulus of equivalent smeared material in the fiber direction (1) and normal to fiber direction (2), within the laminate plane, respectively.  $\nu_{12}=-\varepsilon_1/\varepsilon_2$  and  $G_{12}$ , respectively, represent the in-plane Poisson's ratio and shear modulus, and  $\rho$  is the mass density. The axial, coupling and torsional stiffnesses of the composite tube ( $\kappa_1$ ,  $\kappa_{12}$ , and  $\kappa_2$ ) were first calculated and compared to those published in [27] in order to validate the approach taken in this research.

Table I presents the stiffness terms for fiber-angles  $\eta=20^\circ$  and  $\eta=60^\circ$  and the variation of the circular tube cross-sectional stiffness coefficients with  $\eta$  is shown in Fig. 4.

TABLE I  
GEOMETRIC AND STIFFNESS PROPERTIES; THE UNIFORM CUS COMPOSITE CIRCULAR TUBE; FIBER ANGLES  $\eta=20^\circ$  AND  $\eta=60^\circ$

Fibre Angle ( $\eta$ )	Axial $\kappa_1$ (N)	Coupling $\kappa_{12}$ (N m)	Torsional $\kappa_2$ (N m <sup>2</sup> )	$I_\alpha$ (kgm)	$m$ (kg/m)
$20^\circ$	4,293,824	-65,012.6	1,842.36		
$60^\circ$	587,432.1	-56,147.8	995.1941	0.00144399	2.23174

The first three natural frequencies of the system for fiber-angles  $\eta=0^\circ$ ,  $\eta=20^\circ$  and  $\eta=60^\circ$  were calculated using the DSM, DFE and FEM models (see Table II).

The DSM and FEM results, respectively, were calculated from the exact theory developed by Banerjee and Butler [6] and the FEM formulation discussed earlier in section II.I of this paper (i.e., based on linear polynomial interpolation functions for both extensional and torsional displacements).

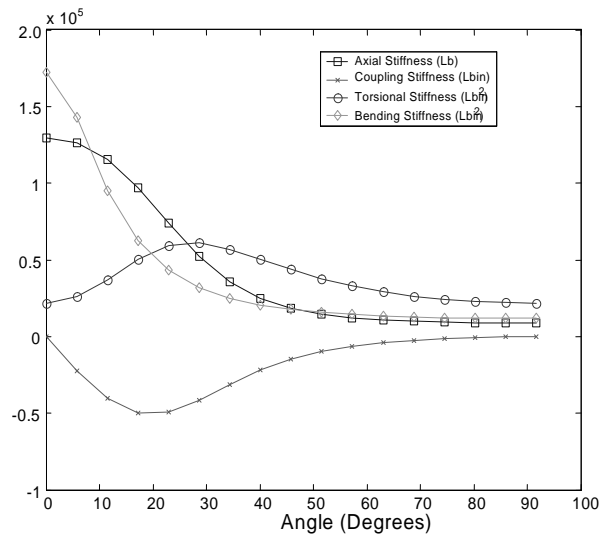


Fig. 4. Stiffness Terms vs Fiber-Angle ( $\eta$ ) for the Uniform CUS Composite Circular Tube

The DSM results were first validated against the published data presented Atiligan *et al.* [27]. The DFE and FEM results cited in the table are all obtained using a 5-element mesh and, as can be seen from Table II, even using this small number of elements the DFE method is able to closely approximate all the three frequencies and results in convergence rates much higher than the FEM.

One should note that the frequency values of [27] were read from a graph and therefore are not overly accurate, explaining some of the discrepancy between them and those obtained from DSM/exact, DFE and FEM models. The first three extension-torsion coupled frequencies for different fiber angles ( $0^\circ < \eta < 90^\circ$ ) are shown in Fig. 5. The results are confirmed by those published in [27]. The variation of the first three 'pure' bending frequencies with  $\eta$  was also determined and the resulting graph was found to be in agreement with the similar one published in the literature [27] allowing for further verification of the bending model used for a wide range of fiber-angles ( $0^\circ < \eta < 90^\circ$ ).

TABLE II  
COUPLED NATURAL FREQUENCIES; COMPOSITE CIRCULAR TUBE (HZ)

Frequency	DSM	DFE	FEM	Ref. [27]
$\eta=0^\circ$				
$\omega_i$				
$i=1$	196.80	196.80	197.59	200
$i=2$	590.40	590.40	612.37	595
$i=3$	941.80	941.80	945.63	945
$\eta=20^\circ$				
$\omega_i$				
$i=1$	202.70	203.18	203.57	205.00
$i=2$	608.20	620.15	630.89	605.00
$i=3$	798.20	800.10	801.50	810.00
$\eta=60^\circ$				
$\omega_i$				
$i=1$	213.65	213.70	214.53	215
$i=2$	294.09	294.16	295.31	300
$i=3$	640.96	642.29	664.87	630

The DFE and FEM convergence rates for  $\eta=60^\circ$  are shown in Figs. 6. Similar convergence tests were also carried out for  $\eta=20^\circ$  [25]. Generally speaking, the DFE method results in much higher convergence rates; for  $\eta=20^\circ$ , the DFE converged to the exact first three modes almost twice faster than FEM. For  $\eta=60^\circ$ , the difference is even more pronounced and DFE convergence rates for the first two modes are found to be more than ten times higher than those obtained from FEM, while maintaining its superiority for the third mode. The first three natural modes for  $\eta=0^\circ$  and  $\eta=60^\circ$  are shown in Figs. 7 and 8, respectively. As can be seen from Figs. 7, when  $\eta=0^\circ$  the modes are uncoupled and purely torsional (see the corresponding natural frequencies presented in Table II).

The modes were also plotted for  $\eta=20^\circ$  [25]. Natural modes reveal strong dependence of natural frequencies and modes on ply angle ( $\eta$ ) and demonstrate the importance of accurately accounting for this coupling within the analysis.

#### IV. Concluding Remarks

The aim of this investigation was to demonstrate the applicability of the DFE method for the free vibration analysis of composite beams exhibiting materially coupled linear torsion-extension.

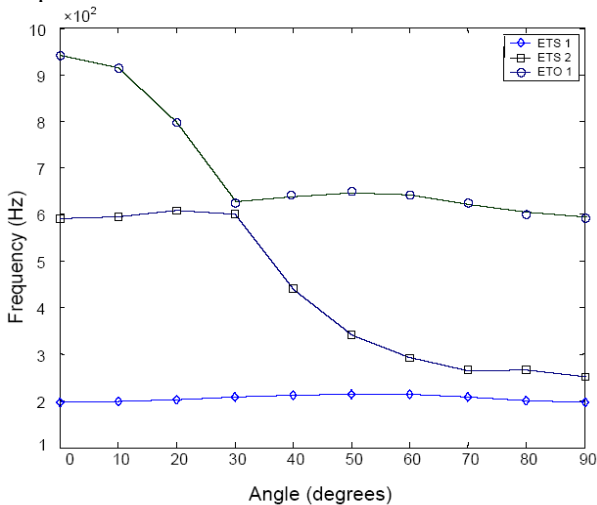


Fig. 5. First Three Extension-Torsion (ET) Coupled Frequencies vs Ply Fiber-Angle ( $H$ ) for the Uniform CUS Composite Circular Tube

The concept of dynamic trigonometric shape functions (DTSFs) and the FEM methodology were used to find the frequency-dependent dynamic stiffness matrices of the system.

The DFE results were found to be in excellent agreement with the theories and data reported in the literature. Comparing to the conventional FEM, the DFE led to greatly faster convergence rates. The use of DTSFs is found to improve the DFE's accuracy over conventional FEM methods. In addition, the DFE is directly applicable to piecewise uniform (stepped) configurations, as well. It is also possible to extend the proposed method to composite beams with nonuniform geometry and/or variable properties, where uniform Saint Venant torsion theory is applicable.

This fact distinguishes the DFE from the DSM. The DFE presented in this paper does not account for nonuniform torsion or warping effects governed by higher order equations. Further research is currently being carried out to include these effects in the DFE model and analysis.

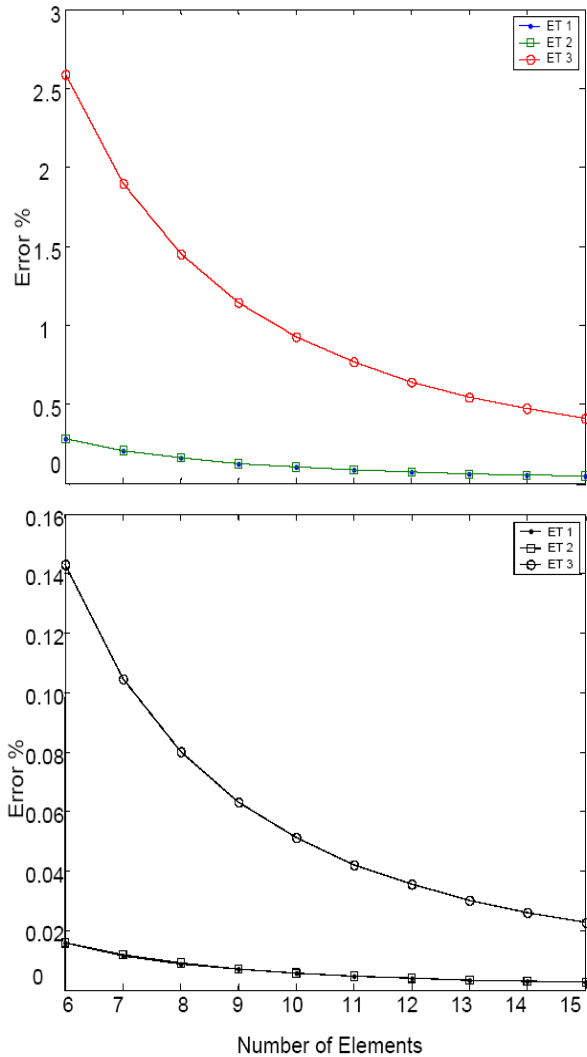


Fig. 6. FEM and DFE Convergence Results For the First Three Frequencies of the Uniform CUS Composite Circular Tube ( $\eta=60^\circ$ )

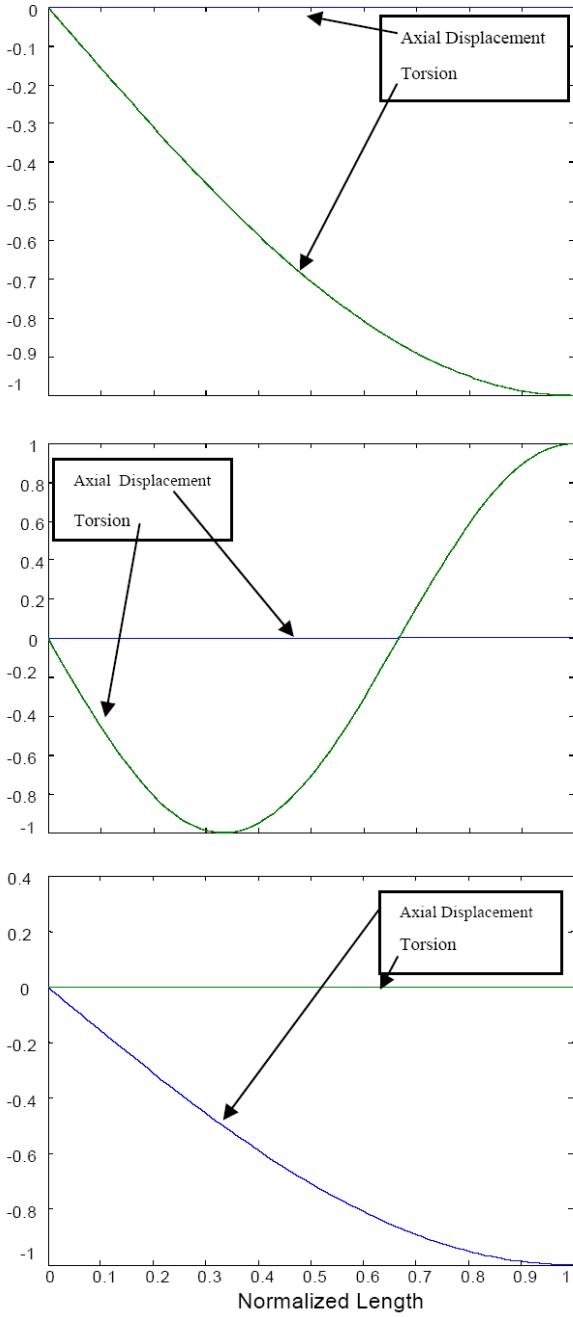


Fig. 7. First Three Natural Modes of Vibration for A Uniform CUS Composite Circular Tube ( $\eta=0^\circ$ )

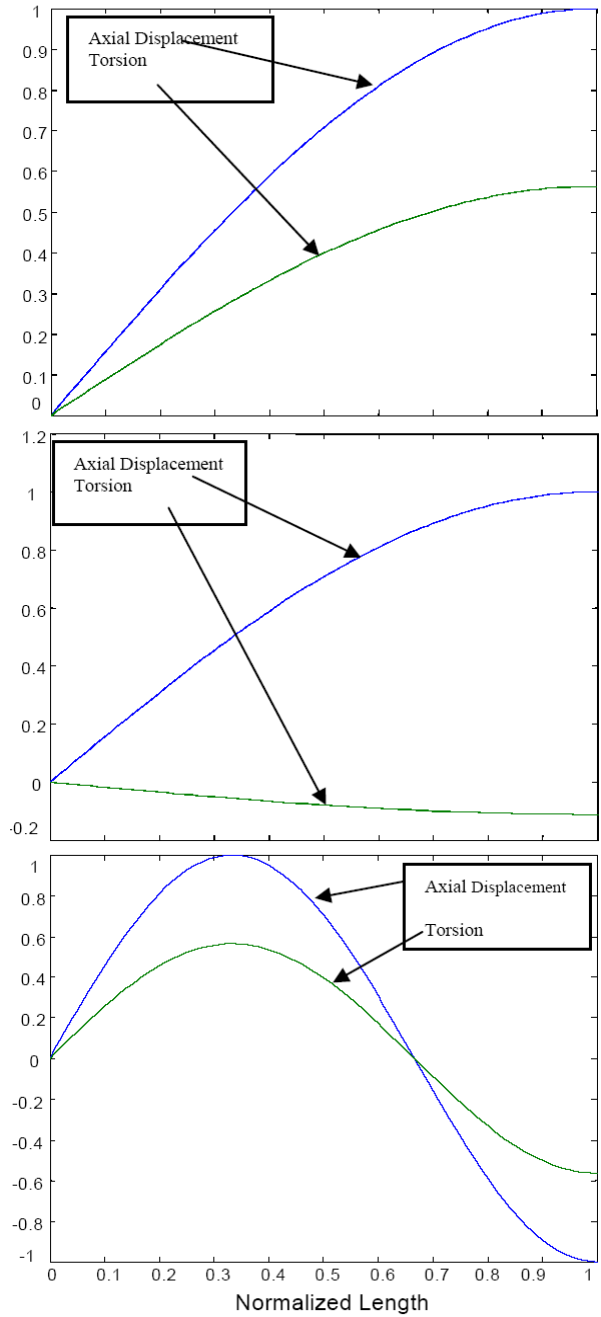


Fig. 8. First Three Natural Modes of Vibration for A Uniform CUS Composite Circular Tube ( $\eta=90^\circ$ )

### Appendix

#### Appendix I. Derivation of CUS Composite stiffness coefficients.

The geometric properties for circular tube (or box-beam) are:

$$A_{CircularTube} = \pi \left( r - \frac{t}{2} \right)^2 \quad (29)$$

$$I_{CircularTube} = 2\pi \left( r - \frac{t}{2} \right)^3 \quad (30)$$

$$m_{CircularTube} = 2\pi\rho r t \quad (31)$$

$$I_{CircularTube} = 2\pi\rho r t^3 \quad (32)$$

where  $m$  and  $I$  are the mass per unit length and the mass moment of inertia per unit length, respectively. For CUS configuration beams which exhibit extension-torsion coupled behaviour the stiffness parameters of interest are  $\tau_1=C_{11}$ ,  $\tau_{12}=C_{12}$  and  $\tau_2=C_{22}$ .

Since for a CUS configuration beam the effective reduced stiffness terms 'A(s)', 'B(s)' and 'C(s)' are

constant around the cross section and therefore the cross sectional stiffness are:

$$C_{11} = \oint \left( A - \frac{B^2}{C} \right) ds + \frac{\left[ \oint \left( \frac{B}{C} \right) ds \right]^2}{\oint \left( \frac{1}{C} \right) ds} = Al \quad (33)$$

$$C_{12} = \frac{\oint \left( \frac{B}{C} \right) ds}{\oint \left( \frac{1}{C} \right) ds} A_e = BA_e \quad (34)$$

$$C_{22} = \frac{1}{\oint \left( \frac{1}{C} \right) ds} A_e^2 = \frac{C}{l} A_e^2 \quad (35)$$

where  $l$  is the length of the centreline of the cross section,  $A_e$  is the area enclosed by the contour, and:

$$A = A_{11} - A_{12}^2 / A_{22} \quad (36)$$

$$B = 2(A_{12}A_{26} / A_{22} - A_{16}) \quad (37)$$

$$C = 4(A_{66} - A_{26}^2 / A_{22}) \quad (38)$$

with the in-plane laminate stiffness coefficients,  $A_{ij}$ , defined as:  $A_{ij} = \sum_{k=1}^{NOL} \bar{Q}_{ij} h_k$  where 'NOL' is the total number of lamina which make up the laminate and ' $h_k$ ' is the thickness of each individual lamina ' $k$ '. The lamina transformed reduced stiffnesses,  $\bar{Q}_{ij}$ , are functions of the in-plane lamina reduced stiffness terms,  $Q_{ij}$ , defined using the plane stress assumption and the anisotropic nature of the material as given by [19].

Since this analysis is contour based it is applicable to any closed-section thin-walled CUS beam.

#### Appendix II. Wittrick-Williams Method.

The Wittrick-Williams (W-W) algorithm is a simple method of calculating the number of natural frequencies of a system that are below a given trial frequency value.

The method exploits the bisection method and the Sturm sequence properties of the dynamic stiffness matrix to converge on any particular natural frequency of the system, to any desired accuracy. This allows one to solve for any specific frequency number without having to solve for all previous frequencies, which is the requirement of some linear eigenvalue solvers. Consequently, the corresponding modes can be evaluated [21], [23], [24]. The basic equation of the W-W method is [16]:

$$J = J_o + \text{sign} \left[ \bar{K}(\omega)^\Delta \right] \quad (39)$$

where ' $J$ ' is the number of natural frequencies below the trial value and ' $J_o$ ' is defined by:

$$J_o = \sum_{m=1}^{NOE} J_m \quad (40)$$

' $J_m$ ' is the number of clamped-clamped natural frequencies of any component member (element) of the structure that lies below the trial frequency.

$\text{sign} \left[ \bar{K}(\omega)^\Delta \right]$  in (26) is the number of negative elements on the leading diagonal of  $\left[ \bar{K}(\omega)^\Delta \right]$ , where  $\left[ \bar{K}(\omega)^\Delta \right]$  is the upper triangularized matrix found by using Gaussian elimination (with no column pivoting [16]) on  $\left[ \bar{K}(\omega) \right]$  evaluated at the trial value.

One should note that the iterative nature of the bisection solver used in conjunction with this method and the requirement of the evaluation of the stiffness matrix at each trial frequency makes it require increased computational time when compared to most linear eigenvalue methods.

#### Appendix III. Clamped-Clamped Natural Frequencies.

In order to make use of the W-W method at each trial frequency, one must determine the CL/CL natural frequencies of vibration for all the component members of the discretized system. In order to determine these frequencies one can exploit the exact solution for the CL/CL extension-torsion coupled natural frequencies given by Banerjee and his colleagues [6], [7].

The CL/CL natural frequencies for an extension-torsion coupled element correspond to the value of ' $\omega$ ' that yield infinities in the DSM frequency dependant stiffness matrix. In other words, the term ' $\Delta$ ' which occurs in the denominator should be set to zero ( $\Delta=0$ ), where [6], [7]:

$$\Delta = (k_{\beta_1} - k_{\beta_2}) \sin \beta_1 \sin \beta_2 = 0 \quad (41)$$

and:

$$\kappa_{\beta_1} = \frac{\kappa_{12} \beta_1^2}{(I \omega^2 L^2 - \kappa_2 \beta_1^2)} = \frac{(m \omega^2 L^2 - \kappa_1 \beta_1^2)}{\kappa_{12} \beta_1^2} \quad (42)$$

$$\kappa_{\beta_2} = \frac{\kappa_{12} \beta_2^2}{(I \omega^2 L^2 - \kappa_2 \beta_2^2)} = \frac{(m \omega^2 L^2 - \kappa_1 \beta_2^2)}{\kappa_{12} \beta_2^2} \quad (43)$$

$$\left. \begin{matrix} \beta_1^2 \\ \beta_2^2 \end{matrix} \right\} = \frac{\omega^2 L^2 \left[ (\kappa_1 I + \kappa_2 m) \pm \left\{ (\kappa_1 I - \kappa_2 m)^2 + 4mI\kappa_{12}^2 \right\}^{1/2} \right]}{2(\kappa_1 \kappa_2 - \kappa_{12}^2)} \quad (44)$$

The term  $(k_{\beta_1} - k_{\beta_2})$  in Eq. (28) can not be equal to zero, therefore  $\sin \beta_1 \sin \beta_2$  must be equal to zero. The solution to this equation is easily found from inspection and is given by:

$$\beta_1 = n\pi \text{ or } \beta_2 = n\pi \quad (45)$$

The solution for the CL/CL frequencies can now be obtained by substituting (32) into Eq. (31) and are given by [6], [7]:

$$\omega_{\beta_1}^2 = \frac{2(\kappa_1\kappa_2 - \kappa_{12}^2)n\pi}{L^2 \left[ (\kappa_1 I_\alpha + \kappa_2 m) + \left\{ (\kappa_1 I_\alpha - \kappa_2 m)^2 + 4m I_\alpha \kappa_{12}^2 \right\}^{1/2} \right]} \quad (46)$$

$$\omega_{\beta_2}^2 = \frac{2(\kappa_1\kappa_2 - \kappa_{12}^2)n\pi}{L^2 \left[ (\kappa_1 I_\alpha + \kappa_2 m) - \left\{ (\kappa_1 I_\alpha - \kappa_2 m)^2 + 4m I_\alpha \kappa_{12}^2 \right\}^{1/2} \right]} \quad (47)$$

## Acknowledgements

The authors wish to acknowledge the support provided by Natural Sciences and Engineering Research Council of Canada (NSERC) and Ryerson University.

## References

- [1] M.W. Nixon, Extension-twist coupling of composite circular tubes with application to tilt rotor blade design. *Proceedings of 28<sup>th</sup> AIAA/AHS/ASME/ASCE/ASC Structures, Structural Dynamics & Materials Conference, Monterey (1987)*, 295-303.
- [2] O. Song and L. Librescu, Free vibration and aeroelastic divergence of aircraft wings modelled as composite thin-walled beams, *Proceedings of the 32<sup>nd</sup> AIAA/AHS/ASME/ASCE/ASC Structures, Structural Dynamics & Materials Conference, Baltimore, Maryland (1991)*, 2128-2136.
- [3] R. Chandra and I. Chopra, Structural behavior of two-cell composite rotor blades with elastic couplings. *AIAA Journal* 30(12) (1992), 1914-1921.
- [4] C.M. Bothwell, R. Chandra and I. Chopra, Torsional actuation with extension-torsion composite coupling and a magnetostrictive actuator. *AIAA Journal* 33(4) (1995), 723-729.
- [5] E.C. Smith, Vibration and flutter of stiff-inplane elastically tailored composite rotor blades. *Proceedings of the 34<sup>th</sup> AIAA/AHS/ASME/ASCE/ASC Structures, Structural Dynamics & Materials (SDM) Conference, La Jolla, California (1993)*.
- [6] J.R. Banerjee and R. Butler, Coupled Extensional-Torsional Vibration of Composite Beams- An Exact Method, *Proceedings of the 35<sup>th</sup> AIAA/ASME/ASCE/AHS/ASC Structures, Structural Dynamics, & Materials Conference, Hilton Head, S. Carolina (1994)*, 147-154.
- [7] J.R. Banerjee and F.W. Williams, An Exact Dynamic Stiffness Matrix for Coupled Extensional-Torsional Vibration Of Structural Members, *Computers & Structures* 50 (1994), 161-166.
- [8] K. Bhaskar and L. Librescu, Buckling under axial compression of thin-walled composite beams exhibiting extension-twist coupling.

- Computers & structures* 31 (1995), 203-212.
- [9] CES Cesnik, D.H. Hodges and M.J. Patil, Aeroelastic analysis of composite wings, *Proceedings of the 37<sup>th</sup> AIAA/ASME/ASCE/AHS/ASC Structures, Structural Dynamics & Materials Conference & Exhibit, Salt Lake City, UT (1996)*, 1113-1123 (Technical Papers. Pt. 2).
- [10] J.B. Kosmatka and RC. Lake, Extension-twist behavior of initially twisted composite spars for tilt-rotor applications. *Proceedings of the 37<sup>th</sup> AIAA/ASME/ASCE/AHS/ASC Structures, Structural Dynamics, & Materials Conference. Reston, VA (1996)*, 2175-2184 (Technical Papers. Pt. 4).
- [11] D.H. Hodges, Torsion of pretwisted beams due to axial loading. *ASME Journal of Applied Mechanics* 47 (1980), 393-397.
- [12] S. Krenk, The torsion-extension coupling in pretwisted elastic beams. *Int. J. Solids Structures* 19(1) (1983), 67-72.
- [13] G Cutri and A. Risitano, Coupled free, torsional and axial vibration of pre-twisted bars. *Meccanica* 14(3) (1979), 157-162.
- [14] H.H. Chen and K.M. Hsiao, Coupled axial-torsional vibration of thin-walled Z-section beam induced by boundary conditions. *Thin-walled Structures* 45 (2007), 573-583.
- [15] K-C Liu, J. Friend and L. Yeo, Vibration analysis of pretwisted beams for the design of hybrid axial-torsional transducer. *CD Proceedings of the 48<sup>th</sup> AIAA/ASME/ASCE/AHS/ASC Structures, Structural Dynamics & Materials Conference, Honolulu, Hawaii (2007)*, 1-20.
- [16] W.H. Wittrick and F.W. Williams, A general algorithm for computing natural frequencies of elastic structures. *Q. J. Mech. Appl. Math.* 24 (1971), 263-284.
- [17] S.M. Hashemi and A. Roach, A Dynamic Finite Element for vibration analysis of composite circular tubes. *Proceedings of the Tenth International Conference on Civil, Structural & Environmental Engineering Computing, B.H.V. Topping, (Editor), Civil-Comp Press, Stirling, United Kingdom, paper 177, 2005.*
- [18] R. Chandra, A.D. Stemple and I. Chopra, Thin-walled composite beams under bending, torsional and extensional loads. *Journal of Aircraft* 27 (7) (1990), 619-626.
- [19] M.W. Hyer, *Stress Analysis of Fibre-Reinforced Composite Materials* (WCB/McGraw-Hill Company Inc., 1998)
- [20] F.W. Williams, W.P. Howson and J.R. Banerjee, Natural frequencies of members with coupled extensional torsional motion. A physical approach. *Journal of Sound & Vibration* 165(2) (1993), 373-375.
- [21] S.M. Hashemi and M.J. Richard, Free vibrational analysis of axially loaded bending-torsion coupled beams: a dynamic finite element, *Computers & Structures* 77 (2000), 711-724.
- [22] K.J. Bathe, *Finite element procedure in engineering analysis*. (Englewood Cliffs, NJ: Prentice-Hall, 1982).
- [23] S.M. Hashemi, M.J. Richard and G. Dhatt, A new dynamic finite element (DFE) formulation for lateral free vibrations of Euler-Bernoulli spinning beams using trigonometric shape functions, *Journal of Sound & Vibration* 220(4) (1999), 601-629.
- [24] S.M. Hashemi and M.J. Richard, Natural frequencies of rotating uniform beams with coriolis effects. *Journal of Vibration & Acoustics* 123(4) (2001), 444-455.
- [25] A. Roach, *Free vibration analysis of extension-torsion coupled elements using a dynamic finite element (DFE) formulation*. MEng. Thesis, Ryerson University, 2005.
- [26] E.A. Armanios, A.M. Badir and V. Berdichevsky, Theory of Anisotropic Thin-Walled Closed-Cross-Section Beams. *Composite Engineering* 2(5-7) (1992), 411-432.
- [27] A.R. Atiligan, M.V. Fulton, D.H. Hodges and L.W. Rehfield, Free-vibration analysis of composite beams. *Journal of American Helicopter Society* 36(3) (1991), 36-47.

## Authors' information

Department of Aerospace Engineering, Ryerson University, Toronto (ON), Canada M5B 2K3.

Web page:

<http://www.ryerson.ca/aerospace/research/Research%20profiles/hashe mi.html>

E-mail: [smlhashem@ryerson.ca](mailto:smlhashem@ryerson.ca)



**Seyed M. Hashemi** was born in Kashan, Iran, June 2<sup>nd</sup>, 1966. Awarded B.Sc in Mechanical Engineering, Sharif University of Technology, Tehran, Iran, in 1990, DEA en Mécanique, Ecole Centrale de Lille, Université de Lille I, Lille, France, in 1992, and PhD in Mechanical Engineering, Laval University, Québec (QC), Canada, in 1998. He is the main developer of

the DFE formulation and has (co)-authored some twenty journal papers, several chapters in books and edited volumes, and around fifty conference papers on DFE applications in the areas of structural dynamics, vibration, composite and sandwich beam-structures, and the modeling of MEMS devices. Dr. Hashemi is an associate professor, Department of Aerospace Engineering, Ryerson University, Toronto (ON), Canada, an Adjunct Professor, Department of Mechanical and Mechatronics Eng., University of Waterloo, Waterloo (ON), Canada, a licensed Professional Engineer in Ontario, Canada, and a member of AIAA.

**Andrew Roach** was born in Brampton, Canada, August 25<sup>th</sup> 1979. Awarded B.Eng. in Aerospace Engineering from Ryerson University, Toronto, Canada in 2004, and M.Eng. in Mechanical Engineering from Ryerson University, Toronto, Canada in 2006. He has assisted Dr. Hashemi and contributed to the development and application of the DFE method in the free vibration analysis of extension-torsion coupled structural elements and systems.



*Praise Worthy Prize*



2036-9921(201607)7:4;1-V